Universidade de São Paulo
Escola Politécnica
Departamento de Engenharia Química

Cleiton de Souza Beraldo

A numerical investigation of a fixed bed CO_2 adsorption process using Phase Change Materials

São Paulo
2022

CLEITON DE SOUZA BERALDO

A numerical investigation of a fixed bed CO_2 adsorption process using Phase Change Materials

Versão Corrigida

Dissertação apresentada à Escola Politécnica da Universidade de São Paulo referente à obtenção do título de Mestre em Ciências.

Área de Concentração: Engenharia Química

Orientador: Prof. Dr. Marcelo Martins Seckler

São Paulo

2022

Este exemplar foi revisado e corrigido em relação à versão original, sob responsabilidade única do autor e com a anuência de seu orientador.

São Paulo, _____ de _____ de _____

Assinatura do autor: _____

Assinatura do orientador: _____

Catalogação-na-publicação

Beraldo, Cleiton
Estudo numérico de um processo de adsorção de CO2 em leito fixo usando Materiais de Mudança de Fase / C. Beraldo -- versão corr. -- São Paulo, 2022.
87 p.

Dissertação (Mestrado) - Escola Politécnica da Universidade de São Paulo. Departamento de Engenharia Química.

1.Adsorção 2.Energia térmica 3.Leito fixo 4.Materiais de mudança de fase 5.Captura e sequestro de carbono I.Universidade de São Paulo. Escola Politécnica. Departamento de Engenharia Química II.t.

CLEITON DE SOUZA BERALDO

Dissertação apresentada à Escola Politécnica da Universidade de São Paulo referente à obtenção do título de Mestre em Ciências.

São Paulo

2022

“All things dissolve in time”

Lyric from “Dreams Wash Away” by Joe Wong in “The Midnight Gospel”

DEDICATÓRIA

Aos que compartilham comigo a vida

Aos que celebram a natureza

AGRADECIMENTOS

Gostaria de agradecer ao meu orientador, Prof. Dr. Marcelo Martins Seckler, por toda a ajuda e paciência na elaboração deste trabalho.

Agradecimentos especiais ao Prof. Dr. José Luís de Paiva, que teve papel decisivo na compreensão da complexidade relacionada ao assunto estudado.

Agradeço à Profa. Dra. Diana Cristina Silva de Azevedo e ao Prof. Dr. Yuri Nascimento Nariyoshi pelos valiosos conselhos e sugestões práticas que deram durante o exame de qualificação.

Muito obrigado ao Enzo Sampronha pela amizade e pela inestimável contribuição para este projeto.

Gostaria de agradecer a ajuda técnica inigualável e as lições compartilhadas pelo M.Sc. Adriano Bonangelo Costa.

Sou profundamente grato a todas as pessoas que facilitaram os dias ao longo desses anos, desde os adoráveis colegas até os profissionais incríveis.

Também gostaria de agradecer à Universidade de São Paulo por oferecer seu espaço para valorizar a pesquisa; e CAPES e FAPESP pelo apoio financeiro.

E aos meus amigos, obrigado por todo o apoio sincero, isso significa muito, obrigado.

RESUMO

Beraldo, Cleiton de Souza. Estudo numérico de um processo de adsorção de CO_2 em leito fixo usando Materiais de Mudança de Fase. 2022. 87 p. Dissertação (Mestrado em Engenharia Química) – Escola Politécnica da Universidade de São Paulo. Departamento de Engenharia Química. São Paulo, 2022.

O interesse pela adsorção no contexto de Sequestro e Captura de Carbono (CCS) tem aumentado nos últimos anos devido ao baixo consumo de energia exigido pelo processo, em comparação com a mais conhecida rota de absorção. A fim de reduzir ainda mais a energia requerida pela adsorção e aumentar a capacidade de adsorção, foram propostas medidas para neutralizar o comportamento exotérmico indesejado dos processos de adsorção, como elementos de troca térmica ativos inseridos no leito de adsorção e materiais de mudança de fase (PCM). Este último oferece grande potencial por ser capaz de armazenar quantidades substanciais de energia. Neste trabalho o objetivo é analisar o comportamento de um sistema de adsorção de CO_2 em leito fixo com PCM e fornecer uma interpretação fenomenológica simples. O leito é preenchido com carvão ativado ou zeólita como adsorvente, e de parafina como material de mudança de fase. O modelo matemático para PCM em leito fixo proposto por Schumman, baseado em balanços de massa e energia, foi modificado para incluir as expressões de fenômenos de transporte, equilíbrio termodinâmico e cinética de adsorção. O modelo foi validado com dados experimentais da literatura e os resultados da solução numérica foram utilizados para analisar o desempenho térmico da etapa de adsorção. Os estudos revelaram que no uso de apenas 1% de PCM houve um aumento da capacidade de adsorção de CO_2 em 10% em volume total de gás adsorvido, devido à redução da temperatura máxima do processo em 2 ºC. Para ser o mais eficaz, a zona de transferência de calor do material de mudança de fase se alinhe com a curva de ruptura do processo de adsorção.

Palavras-chave: Adsorção. Energia térmica. Leito fixo. Materiais de mudança de fase. Captura e sequestro de carbono.

ABSTRACT

Beraldo, Cleiton de Souza. A numerical investigation of a fixed bed CO_2 adsorption process using Phase Change Materials. 2022. 87 p. Dissertation (Master in Chemical Engineering) – Polytechnic School. University of São Paulo. Department of Chemical Engineering. Sao Paulo, 2022.

Interest in adsorption in the context of Carbon Capture and Storage (CCS) has increased in recent years due to the low energy consumption required, as compared to the more well-established route of absorption. In order to reduce even more the energy required by adsorption and to increase the specific adsorption capacity, measures have been proposed to counteract the undesired exothermic behavior of adsorption processes, such as U-tubes inserted on the adsorption bed and phase change materials (PCM). The latter offers great potential of storing substantial amounts of energy. In this work, the aim is to analyze the behavior of a fixed bed CO_2 adsorption system with PCM and provide a comprehensive interpretation to explain the phenomenon. The bed is filled with activated carbon or zeolite as adsorbent and paraffin wax as phase change material. The mathematical model for PCM in fixed bed proposed by Schumman, based on balances of mass and energy, has been modified to include the expressions of transport phenomena, thermodynamic equilibrium and adsorption kinetics. The model was validated with experimental data from literature and the results from the numerical solution were used to analyze the thermal performance of the charging mode of the adsorption process and. The studies revealed a increase of the theoretical CO_2 adsorption in capacity by 10% in total volume of gas adsorbed, due to the reduction of the maximum temperature of the process by 2 ºC. To be the most effective, the heat transfer interval of the phase change material aligns with the adsorption breakthrough curve.

Keywords: Adsorption. Latent heat thermal energy storage. Fixed bed. Phase change material. CCS.

LIST OF FIGURES

LIST OF TABLES

ABBREVIATIONS

1D	one-dimensional
AC	activated carbon
BC	boundary condition
CCS	carbon capture and storage
EHTI	effective heat transfer interval
Fig.	figure
HTF	heat transfer fluid
HTI	heat transfer interval
LTES	latent thermal energy storage
MOF	metal-organic frameworks
MTZ	mass transfer zone
PCM	phase change materials
PSA	pressure swing adsorption
SLPM	standard liter per minute
STP	standard temperature and pressure
TES	thermal energy storage
TSA	temperature swing adsorption
vs	versus
VSA	vacuum swing adsorption

NOMENCLATURE

A_S	cross-sectional area of PCM shell (m^2)
C	adsorbate concentration in gas phase (mol m^{-3})
c_i	y_iC, gas phase concentration of species i (mol m^{-3})
$C_{p,A}$	adsorbent heat capacity (J kg^{-1} K^{-1})
$C_{p,F}$	heat capacity of fluid phase (J mol^{-1} K^{-1})
$C_{p,G}$	gas heat capacity at constant pressure (J mol^{-1} K^{-1})
$C_{p,PCM}$	PCM heat capacity (J kg^{-1} K^{-1})
$C_{p,S}$	PCM shell heat capacity (J kg^{-1} K^{-1})
$C_{p,W}$	column wall specific heat (J kg^{-1} K^{-1})
$C_{v,G}$	gas heat capacity at constant volume (J mol^{-1} K^{-1})
d_A	adsorbent particle diameter (m)
D_K	Knudsen diffusivity (m^2 s^{-1})
D_m	molecular diffusivity (m^2 s^{-1})
$d_{PCM,int}$	PCM internal diameter (m)
d_{Wext}	column wall external diameter (m)
d_{Wint}	column wall internal diameter (m)
D_z	axial dispersion coefficient (m^2 s^{-1})
F_{in}	fluid flow-rate at the bed inlet (m^3 s^{-1})
g	gravity acceration (m s^{-2})
h_{FPCM}	heat transfer coefficient between HTF and PCM (W m^{-2} K^{-1})
h_{GA}	film heat transfer coefficient between gas and adsorbent (W m^{-2} K^{-1})
h_{GW}	heat transfer coefficient between packed bed and column wall (W m^{-2} K^{-1})
H_{PCM}	PCM enthalpy (J kg^{-1})
K_{eq}	Toth constant for adsorption equilibrium (Pa^{-1})
K_{eq0}	adsorption equilibrium constant at infinite dilution (Pa^{-1})
k_{ext}	external air conductivity (W m^{-1} K^{-1})
k_F	effective thermal conductivity of heat transfer fluid and bed (W m^{-1} K^{-1})
$k_{LDF,i}$	adsorption rate constant for species i (s^{-1})
k_{PCM}	thermal conductivity of PCM (W m^{-1} K^{-1})

k_W	column wall conductivity (W m^{-1} K^{-1})
L_{PCM}	total PCM length (m)
L_W	total bed length (m)
l_W	column wall thickness (m)
M_i	molecular weight of component *i* (kg $kmol^{-1}$)
P	operation pressure (Pa)
p	y_iP, partial pressure (Pa)
Pe	Peclet number
Pr	Prandtl number
q_{eq}	adsorbed concentration in equilibrium with the fluid phase (mol kg^{-1})
$F_{G,in}$	gas inlet flow rate (m^3 s^{-1})
q_i	amount adsorbed of species *i* (mol kg^{-1})
q_m	maximum adsorbed concentration (mol kg^{-1})
r	bed radial direction (m)
R	gas constant (J mol^{-1} K^{-1})
Ra	Rayleigh number
Re	Reynolds number
R_{extPCM}	convective thermal resistance external to PCM (kg K W^{-1} m^{-2})
R_{intPCM}	resistance due to the solidified/melted PCM layer inside the capsule (kg K W^{-1} m^{-2})
r_{PCM}	PCM radius (m)
r_{pore}	average pore radius (m)
R_S	resistance due to conduction of the PCM shell (kg K W^{-1} m^{-1})
r_S	PCM shell radius (m)
Sc	Schmidt number
t	process time (s)
T	temperature (K)
T_A	adsorbent temperature (K)
T_B	bed temperature (K)
T_{ext}	external temperature (K)
T_F	fluid temperature (K)
T_G	gas temperature (K)

T_{in} fluid inlet temperature (K)

T_{mPCM} PCM melting point (K)

T_{PCM} PCM temperature (K)

T_W wall temperature (K)

u_F fluid superficial velocity (m s^{-1})

u_G gas superficial velocity (m s^{-1})

U_{PCM} overall heat transfer coefficient between the packed bed and PCM (W kg^{-1} K^{-1})

U_{Wext} overall heat transfer coefficient between bed wall and environment (W m^{-2} K^{-1})

V_C column volume based on internal wall diameter (m^3)

$V_{f,PCM}$ PCM volume fraction in the column

y_i mole fraction of species *i*

z bed axial direction (m)

Greek letters

α_{ext} air thermal diffusivity at film temperature (m^2 s^{-1})

α_{PCM} ratio between PCM surface area and bed volume (m^{-1})

β thermal expansion coefficient (K^{-1})

ΔH_{ads} isosteric heat of adsorption (J mol^{-1})

ΔH_{PCM} latent heat of PCM paraffin wax (J kg^{-1})

ε_A porosity of the adsorbent particles

ε_B bed void fraction

λ_z effective axial thermal conductivity (W m^{-1} K^{-1})

μ_G gas phase dynamic viscosity (Pa s)

ν_{ext} air kinematics viscosity at film temperature (m^2 s^{-1})

ρ_A particle density (kg m^{-3})

ρ_F heat transfer fluid density (mol m^{-3})

ρ_G gas phase density (mol m^{-3})

ρ_{PCM} PCM particle density (kg m^{-3})

ρ_S PCM shell density (kg m^{-3})

ρ_W column wall density (kg m^{-3})

τ tortuosity

φ_{PCM}	volumetric fraction of PCM capsules in the bed
χ	Toth heterogeneity parameter
ω_{PCM}	PCM liquid volume fraction (m^3 PCM_l m^{-3} PCM_s^{-1})

Subscripts

B	bed
b	breakthrough
CO2	carbon dioxide component
ex	exhaustion
ext	external/surroundings/environment
F	fluid
G/g	gas
i	fluid species
in	inlet
l	liquid
N2	nitrogen component
PCM	phase change material
r	bed radial direction
S	PCM shell
s	solid
sat	saturation
vol.	volume
wt.	weight
z	bed axial direction

CONTENTS

1 Introduction

As joint efforts focus on mitigating the emission of greenhouse gases in the atmosphere, strategies have been proposed to reduce global warming, including a shift to a greener energy consumption and capturing CO_2 from human industrial activity (GIELEN et al., 2019; MARTIN-ROBERTS et al., 2021). Carbon Capture and Storage (CCS) has been studied over the past two decades and technologies developed to tackle the challenge of reliably capturing carbon dioxide at industrial scale (RACKLEY, 2010).

Gas-phase adsorption is among the technologies investigated as a solution to capture CO_2 (ZHANG et al., 2009). A considerable number of adsorbents are known to be applicable for carbon dioxide capture (RACKLEY, 2010), activated carbon being the most employed in these systems and zeolites being studied as a potential successor (BASTOS-NETO; AZEVEDO; LUCENA, 2020).

The undesirable exothermic behavior of adsorption processes reduces the adsorption capacity (BILOÉ; GOETZ; GUILLOT, 2002) hence heat exchange systems have been developed, such as U-tubes (BASUMATARY et al., 2005; RAHMAN et al., 2011; YANG, X. D. et al., 2005) and phase change materials (PCM) (BLAZEK et al., 1990; LI; LI, 2015; RACKLEY, 2010; SAKANAKA et al., 2020) inserted in packed bed adsorption systems. The latter offers great potential because they are capable of storing substantial amounts of energy. The PCM is a passive heat exchanger which absorbs energy as the system heats, reducing the necessity of more complex systems involving active heat exchanger.

In packed bed technology, solid particles are stored in a column where a heat transfer fluid (HTF) flows. To ensure that the thermal energy storage (TES) system is compact and practical, materials with high energy storage density, like PCM filled in capsules, can be applied as the storage element of the packed bed thermal energy. PCM can sustain numerous phase transformation cycles without losing stability (SHARMA et al., 2009).

The PCM can be encapsulated in containers such as tubes, for macroencapsulation processes (magnitude: mm or cm), or each PCM particle is surrounded by a polymeric film in microencapsulation systems (magnitude: μm) to accommodate the material as the phase change occurs to avoid leakage and contamination of the bed (CASINI, 2016).

Various PCM, which can be applied for latent heat storage, consist of organic materials, inorganic materials and eutectic materials. The former is divided into paraffin, fatty acid and polybasic alcohols, whilst the latter is classified into hydrated salt, molten salts and metal or alloy materials (WU, Shaofei et al., 2020). Paraffin is commonly used since its melting point can be easily modified, compared to other materials, making it relevant for a range of applications.

Although some papers have discussed the effect of packed beds with PCM alone to evaluate stability and the heat transfer between PCM and inlet fluid (AMIN; BELUSKO; BRUNO, 2014; BELLAN et al., 2015; CHENG, X.; ZHAI; WANG, 2016; DE GRACIA; CABEZA, 2017; FELIX REGIN; SOLANKI; SAINI, 2009; IZQUIERDO-BARRIENTOS et al., 2016; NALLUSAMY; SAMPATH; VELRAJ, 2006; REGIN; SOLANKI; SAINI, 2008), few studies are available for fixed bed adsorption with phase change materials (CHOI et al., 2019; LI; LI, 2015; RAHMAN et al., 2011; ZIMMERMANN; KELLER, 2006) and even less offer a numerical approach combining the two (HORSTMEIER; GOMEZ LOPEZ; AGAR, 2016; SAKANAKA et al., 2020).

As integrating PCM in an adsorption bed decreases the amount of adsorbent that can be packed in the column there should be an optimal volume fraction of PCM to reach the maximum capacity of total gas adsorbed (SAKANAKA et al., 2020). The PCM acts as a heat sink, thus maximizing the heat transfer between fluid, adsorbent and PCM, which is one of the biggest challenges for the process (HORSTMEIER; GOMEZ LOPEZ; AGAR, 2016).

1.1 Objectives

The major objective of the present work is to understand the phenomena that determine the adsorption capacity of PCM-assisted systems, in fixed bed configuration for CO_2 adsorption. The effects of PCM volumetric fraction in the bed, the radius of the capsule, gas velocity of the working fluid and the inlet temperature of the fluid have been investigated for the charging mode of adsorption.

2 Literature review

2.1 Adsorption fundamentals

Adsorption is defined as the spontaneous tendency of fluid particles to approach and stay in contact with a surface (**Fig. 1**) (BASTOS-NETO; AZEVEDO; LUCENA, 2020).

There are two mechanisms for adsorption to occur, either by physical interaction between the fluid (adsorbate), and the surface (adsorbent), or by a chemical reaction (RUTHVEN, 2001). The key difference between the two is the force involved in the process. For the most common mechanism, physisorption, a weak attraction force such as Van der Waals forces is prevalent, which makes the opposite path, desorption, possible in certain conditions, such as under higher temperature or lower pressures. This is very unlikely in chemisorption since strong chemical bond forces, including covalent and ionic bonds, yield the adsorption path close to irreversibility (POURHAKKAK et al., 2021).

Physical adsorption is always exotermic. Analogous to condensation, there is an increase in molecular density accompanied by dissipation of heat as physical adsorption occurs, thus the enthalpy change is always negative (ERKEY; TÜRK, 2021). This is a crucial fact for the design of unit operation adsorption systems, as it will be discussed in the forthcoming sections.

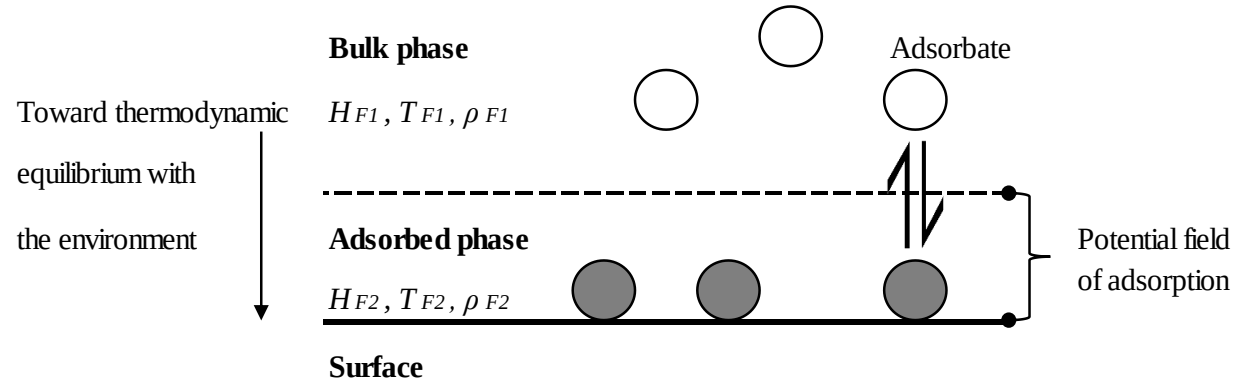

Fig. 1. Gas surface diffusion on physisorbents.
Source: Adapted from Medveď; Černý (2007).

2.2 Adsorption equilibrium

Equilibrium data are expressed as the amount (moles or mass) of adsorbate taken up by a unit mass of the adsorbent (adsorption capacity) at a given temperature and pressure (MOKHATAB; POE; MAK, 2019) and the key aspects that influence equilibrium are (RAY; DAS, 2020): (i) thermophysical properties of adsorbent, (ii) adsorption and desorption cycles which alter the pore structure of the adsorbents leading to changes in their characteristics, (iii) raw material and process used to prepare the adsorbent, and (iv) temperature and presence of impurities or competitive adsorption.

Gas-phase equilibrium isotherms are more available compared to liquid-phase operations (RAY; DAS, 2020). The equilibrium relationship in the vapor phase can be affected by hysteresis and also a loss in adsorption capacity as adsorption and desorption cycles occur. As shown in **Fig. 2**, the hysteresis phenomenon is when the route of adsorption differs from desorption, requiring a lower pressure for the latter path (DONOHUE; ARANOVICH, 1998).

2.3 Adsorption kinetics

Various models of kinetics have been developed (SHAH et al., 2021). Regarding the nature of adsorbents, the pellets have macro and micropores / mesopores. The path made by the adsorbate and the adsorbent network structure is represented in **Fig. 3** for the adsorption step.

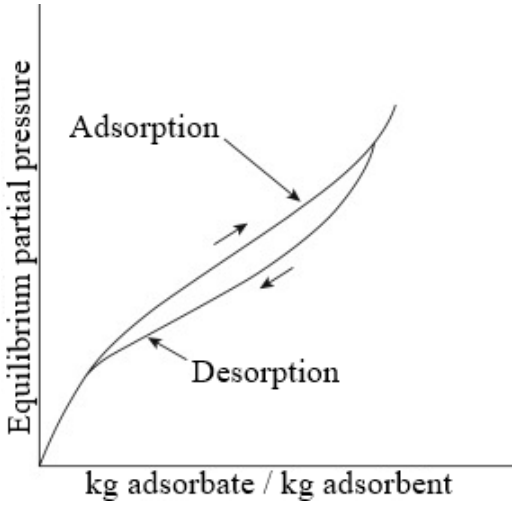

Fig. 2. Hysteresis in adsorption equilibrium.
Source: Adapted from Ray; Das (2020).

First, by diffusion in the meso or micropores, the fluid covers the regions between the adsorbent molecules. Secondly, a film is formed over the adsorbent particle and film diffusion transfer develops from the bulk of the fluid into the particle. Already inside the particle, the adsorbate diffuses through the mesopores in the direction of the micropores (ACKLEY; YANG, 1990). Then, as the fluid molecules diffuse through the micropores, there's a chance for them to get adsorbed by the adsorbent surface.

The three most well-known mechanisms for macropore diffusion are (SHAH et al., 2021): (i) molecular diffusion, (ii) Knudsen diffusion, and (iii) viscous (Poiseuille) diffusion.

The models for rate of adsorption are divided in two groups (HAGHPANAH et al., 2013): (i) adsorption reaction models, and (ii) adsorption diffusion models. The first is for chemisorption mechanisms and assumes that the adsorption happens in one step (QIU et al., 2009). For adsorption diffusion models, three distinct steps occur:

1. External or film diffusion: the diffusion happening over the fluid film around the adsorbent particle;
2. Internal or intraparticle diffusion: the diffusion happening within the adsorbent particle pores;
3. Mass action: the adsorption and desorption are happening between the adsorbent particle active sites and the fluid.

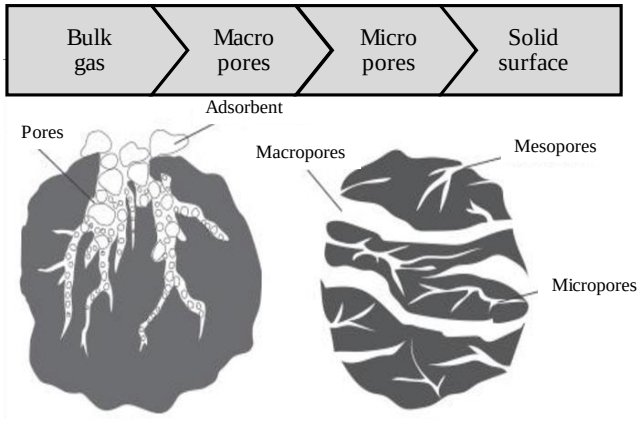

Fig. 3. Gas diffusion path from bulk to adsorbent surface.
Source: Adapted from Gawande et al., (2017).

2.4 Packed bed: adsorption as a separation process

For a specific axial region within a fixed bed, the conditions vary with time. As indicated in **Fig. 4a**. close to the entrance, the bed is saturated with adsorbate and forms the equilibrium zone. Further downstream a mass transfer zone (MTZ) exists, where the adsorbate concentration decreases gradually to zero (PATEL, 2019). The region downstream this point is called the active zone. At the MTZ and the active zone, the bed is capable of removing adsorbate from the gas. As time evolves, the MTZ moves towards the bed outlet.

As the MTZ approaches the end of the bed, adsorbate begins to leave the bed with the effluent. This is observed as a surge in the concentration of adsorbate in the effluent flow with time (SIRCAR; HUFTON, 2000). The well-known concentration versus time curve, commonly obtained in these processes, is represented in **Fig. 4b**, where the breakthrough point indicates the minimum measurable solute fraction in the effluent fluid. The heat generated from adsorption does not dissipate instantly, which increases the temperature locally. This temperature rise can be used as a sign of a breakthrough point (RAY; DAS, 2020).

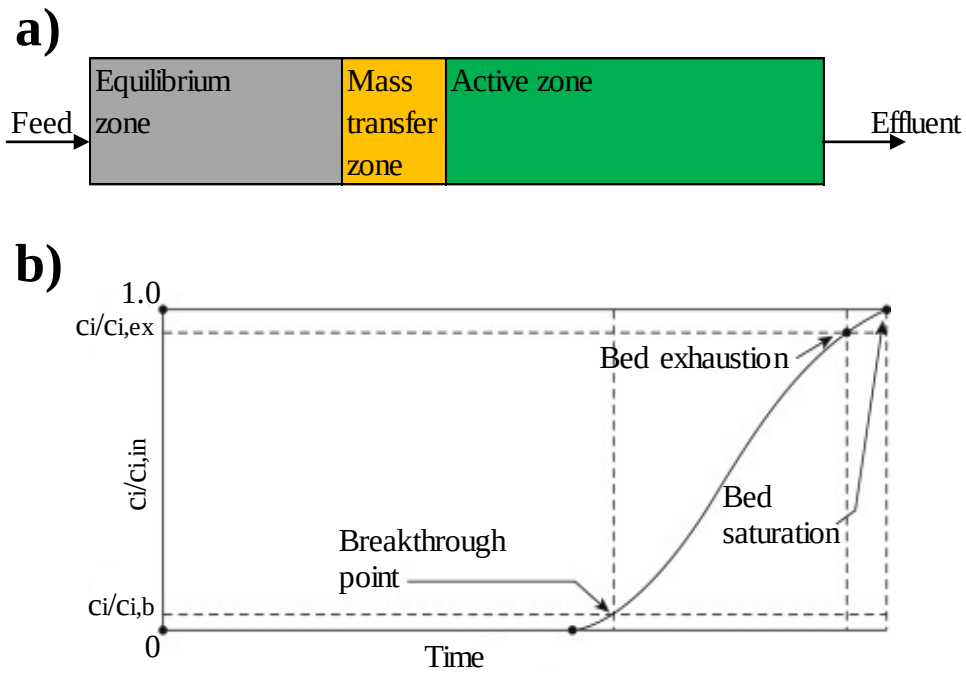

Fig. 4. (a) Classic zones in fixed bed adsorption and (b) breakthrough curve.
Source: Adapted from Ray; Das (2020).

The bed is completely saturated when the adsorbate fraction in the exit of the bed reaches the same value as in the feed. In practice, when this fraction approaches a value close to the feed stream, called the exhaustion point, as shown in **Fig. 4b**, and is typically considered when the effluent concentration is about 95% of the inlet fraction (RAY; DAS, 2020). The key aspects that influence the format of the breakthrough curve are: (i) mechanism of adsorption, (ii) adsorption isotherms, (iii) concentration and speed of adsorbate in feed, and (iv) mass transfer rate - which can be shaped by using different methods, like rising cycle duration or employing small-scale adsorbent particles for faster kinetics.

In adsorption processes, it is crucial to reuse the adsorbent when the breaking point occurs. In regard to the bed regeneration technologies investigated in adsorption, the two most prominent for carbon capture and storage from flue gas are (BEN-MANSOUR et al., 2016):

1. Pressure / Vacuum swing adsorption (PSA / VSA) (KRISHNA, 2012): in PSA, the adsorbate partial pressure can be decreased by reducing the total pressure of the column, or maintaining the total pressure the same and adding an inert diluent in the bed to promote the bed regeneration. It is called VSA if this pressure reduction involves vacuum.
2. Temperature swing adsorption (TSA) (CLAUSSE; BONJOUR; MEUNIER, 2004): in this operation, the adsorption bed is heated by a steam or hot gas feed. Then, a cold gas stream is employed to cool down the bed for the next adsorption step.

2.5 Adsorption bed design

Fixed-bed adsorbers can be designed from experimental breakthrough curve data or by the rigorous solution of transport, thermodynamic and conservation equations (RAY; DAS, 2020).

The experimental method is useful for preliminary design or when full equilibrium and kinetics of adsorption are not available. Otherwise, the rigorous method is preferred as it allows more reliable design and it may be used to new situations such as the inclusion of PCM in the bed, as will be shown later. Detailed descriptions of the breakthrough and the rigorous methods are found in the literature (ARORA; POTŮČEK, 2009).

2.6 Adsorbents for CO_2 capture and the exothermic challenge

Carbon dioxide can be separated from flue gas by applying a variety of physisorbents materials, such as silica gels, alumina, metal-organic frameworks (MOF), porous carbonaceous materials, and zeolites (SAMANTA et al., 2012). For physical adsorption, the selective adsorption of CO_2 by activated carbon (AC) or zeolite 13x, in comparison to N_2, is due to the stronger van der Waals forces linking the adsorbate CO_2, to the adsorbent periphery.

For the success of processes involving CO_2 removal from flue gas, it is critical to develop regenerable sorbents that have high adsorption capacity, selectivity and high mass transfer rate for both adsorption and desorption steps (SIRIWARDANE et al., 2001).

Both AC and zeolite 13x have fast kinetics and the presence of water affects the adsorption capacity negatively for zeolites (SAMANTA et al., 2012). In general, zeolite 13x has greater adsorption enthalpy compared to ACs, due to the latter having weaker interaction with CO_2 (CHUE et al., 1995), and also zeolite 13x has better selectivity, because of the predominance of porous media in activated carbons. Meanwhile, ACs are considered to be low cost compared to other adsorbents and require low regeneration energy, which represents a challenge for zeolite materials, as the adsorbate is strongly attached to the adsorbent sites (SAMANTA et al., 2012).

As adsorption in these materials are strongly determined by temperature, the exothermic behavior of these processes is the key drawback for adsorption capacity (BILOÉ; GOETZ; GUILLOT, 2002) thus heat exchange systems have been developed to decrease the temperature gradient inside packed beds, such as U-tubes inserted on the adsorption bed (RAHMAN et al., 2011; YANG, X. D. et al., 2005) and phase change materials (PCM) (LI; LI, 2015; TOLEDO et al., 2013). The latter offers great potential for latent heat storage systems with materials capable of storing substantial amounts of energy (thermal energy storage, TES).

2.7 Phase change materials

Latent thermal energy storage (LTES) is often linked to phase change materials, which absorb or release a substantial amount of heat as the phase transition (from solid to liquid or the opposite) of the storage material occurs (PAUSE, 2019) and have been mainly applied in solar thermal energy storage, low temperature storage systems for air conditioning, energy efficient

buildings and waste heat recovery systems (REGIN; SOLANKI; SAINI, 2008). The usual layout of the systems used to study the thermal properties of LTES is shown in **Fig. 5**.

Multiple variables have to be considered when projecting a PCM, starting with phase change temperature. The temperature of the system must align with the transition temperature, otherwise phase change may not occur, and only the sensible heat will be stored (NOËL et al., 2016). The next crucial characteristic for a PCM is its phase change latent heat (enthalpy of phase change). To attain the energy storage density required for the process, high latent heat is essential to maximize the heat stored in the phase transition.

2.8 Packed bed PCM systems

Packed and fluidized beds can be applied where heat storing materials may be encapsulated in spheres, cans or other available geometries (ISMAIL; STUGINSKY; STUGINSKY JR, 1999). As optimization of the design and control of these systems is required, many experimental studies have been carried out to assess the thermal properties of LTES technologies for both freezing melting and crystallization paths (DE GRACIA; CABEZA, 2017).

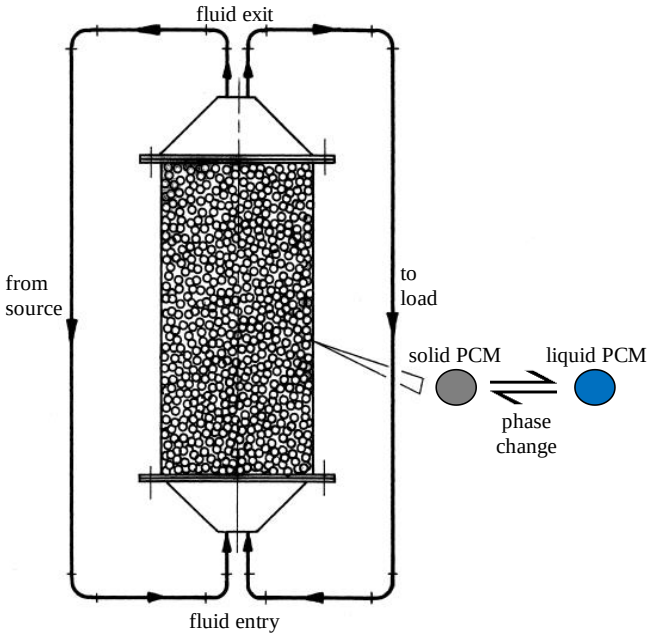

Fig. 5. Generic schematic of packed bed LTES.
Source: Adapted from Ismail et al., (1999).

To investigate the impact of porosity and heat transfer fluid (HTF) flow rate in the performance of a packed bed system, Nallusamy et al., (2006) used paraffin as a PCM, which decreased the size required for the tank. Cho; Choi (2000) also used paraffin in a parametric study to investigate Reynolds number and feed temperature to compute the performance of a packed bed system. The authors concluded that in comparison with a system using water as storage material, the average heat transfer coefficient could reach a value 40% larger for paraffin during both melting and freezing; also, the experiments showed that the melting step is impacted by natural convection developing within the PCM liquid portion.

Although the experiments can offer reliable data for the LTES system, its complex nature and the high cost of the structure makes the use of numerical models crucial to better interpret and learn how to improve the performance (DE GRACIA; CABEZA, 2017). Numerous models have been proposed to numerically predict the performance of packed LTES systems, which assume that PCM spheres fill a cylindrical tank and fluid flows through the bed.

2.9 Packed bed PCM models: an overview

The dynamic models for packed bed LTES are usually separated in two groups (XIA; ZHANG; WANG, 2010): (1) single phase, and (2) two phase models.

It is assumed for the first group, single phase models, that PCM and fluid are represented in one phase thus they are always in thermal equilibrium, which can be appropriate when analyzing packed beds of both high values of thermal capacity and thermal conductivity (ISMAIL; STUGINSKY; STUGINSKY JR, 1999).

For the second group, two phase models, PCM and the HTF have each their own unique phase; hence there is a film separating their interface which the heat transfer is described by Nusselt correlations. This group can be divided into three well-known dynamic models: (1) Schumann's model (SCHUMANN, 1929), (2) continuous solid phase models (BELLAN et al., 2015), and (3) concentric dispersion model (CHENG, X.; ZHAI; WANG, 2016).

In Schumann's model, convection alone drives the heat transfer between the PCM and the HTF phase, in which the energy losses for the surroundings are integrated in the model and both axial and radial heat conduction are neglected. The continuous phase model assumes that the system is composed of a continuous porous medium. The heat conduction in the axial direction, for both PCM and HTF, is taken into account and usually the radial heat conduction is neglected,

hence defining it as a one-dimension axial thermal conduction model (DE GRACIA; CABEZA, 2017). Finally, in the concentric dispersion model the system is composed of a medium of individual particles and the thermal gradient inside the solid phase PCM is considered. A thermal gradient inside the solid PCM particles is assumed, but no inter-particle heat transfer; thus, heat transfer occurs between the fluid PCM and the bed alone (ISMAIL; STUGINSKY; STUGINSKY JR, 1999).

According to Gracia; Cabeza (2017), all four models' predictability is limited because of poor knowledge about the effective thermal conductivity of the porous material and the total heat transfer coefficient between the PCM and the HTF which are commonly calculated using empirical correlations.

The literature presents other models, with varying degree of complexity (AMIN; BELUSKO; BRUNO, 2014; NALLUSAMY; SAMPATH; VELRAJ, 2007). A particular approach was studied by NALLUSAMY; et al. (2007), which can detail the thermal gradients in the PCM spheres' interior, though a two-dimensional CFD is used to solve the model, and a significant computational effort is necessary.

The formulations for the 4 main methods discussed is presented in the following items.

2.10 Single phase PCM model

As both PCM and fluid are represented by one phase, the energy equation can be expressed by (DE GRACIA; CABEZA, 2017):

$$\varepsilon_B C_{p,F} \rho_F \frac{\partial T_B}{\partial t} + (1-\varepsilon_B)\rho_{PCM} \frac{\partial H_{PCM}}{\partial t} + C_{P,F}\rho_F u_F \frac{\partial T_B}{\partial z} = k_{F,z} \frac{\partial^2 T_B}{\partial z^2} + k_{F,r}\left(\frac{\partial^2 T_B}{\partial r^2} + \frac{1}{2}\frac{\partial T_B}{\partial r}\right) \quad (1)$$

Left-hand side of **Eq. 1**, shows the cumulative term of the heat transfer fluid and the PCM, respectively. The convection of the HTF is represented on the last term of the left-hand side of **Eq. 1**. The two terms on the right-hand size are the exchange of thermal energy by conduction in the axial and radial directions, respectively.

Since this methodology considers that PCM and HTF have the same instantaneous temperature, it is only valid for PCM particles with high thermal conductivity, which is a poor hypothesis as these materials are well known for having low thermal conductivity (FARID et al., 2004; ZALBA et al., 2003). Despite this, a single-phase model elaborated by Nagano et al. (2004)

was used to evaluate the performance of an air heat exchanger with PCM granules. The model was validated against experimental data; the use of the model was sustained because of the small dimension of the PCM particles. With the numerical and experimental data, the authors showed that during phase change the amount of heat per unit time and per unit area can be substantial.

2.11 Schumann's model

Schumann's two-phase model considers heat transfer in one dimension and neglects heat conduction in both PCM and fluid phase (SCHUMANN, 1929). The energy equations for the HTF (**Eq. 2**) and the PCM particles (**Eq. 3**) are written:

$$\varepsilon_B C_{p,F} \rho_F \left(\frac{\partial T_F}{\partial t} + u_F \nabla T_F \right) = h_{FPCM} \left(T_{PCM} - T_F \right) - U_{Wext} \left(T_W - T_{ext} \right) \tag{2}$$

$$(1-\varepsilon_B) \rho_{PCM} \frac{\partial H_{PCM}}{\partial t} = h_{FPCM} \left(T_F - T_{PCM} \right) \tag{3}$$

The left hand-side of **Eq. 2** represents the change in fluid enthalpy with time and position, whereas the right hand-side gives the heat loss to the PCM and to the environment. **Eq. 3** describes the gain in enthalpy of the PCM due to heat transfer from the fluid. The term for heat transfer between fluid and PCM is common to both equations

In this model the coefficients are independent of time and position in the bed. Its principal limitation is that the convection is the only driving force in the heat transfer process, whereas thermal diffusion inside the PCM particles is neglected. Since, as previously noted, the PCM has low thermal conductivity, thus the thermal conduction resistance can be relevant during heat transfer. For this reason, some authors have added the conductive thermal resistance at the solid-fluid interface of the model.

Regin; et al., (2009) modified Schumann's model to incorporate the conductive resistive layers at a capsule surrounding the PCM element and the solid particles which may be either entirely solid, as phase change occurs, or totally liquid. Each resistance represented in **Eq. 4** is shown in **Fig. 6**. When the PCM resistances are combined with the convective term, the following overall heat transfer coefficient U_{PCM} results:

$$U_{PCM} = \frac{1}{A_S} \frac{1}{R_{\text{int}\,PCM}(t) + R_S + R_{extPCM}} \tag{4}$$

With this adaptation, the conduction heat within the PCM is considered, even though no discrete counterparts of the capsules are implemented.

2.12 Continuous solid phase model

As the model assumes the system as a continuous medium, there are no thermal gradients inside the PCM. It can be a one or two dimensional to incorporate the heat transfer in the radial direction, which can be useful in a system with low feed flow exposed to environmental losses or in a process with high Reynolds number, although the inclusion of radial direction heat transfer increases the computational effort of the model substantially (ISMAIL; STUGINSKY; STUGINSKY JR, 1999). Again, since it is a two-phase model, **Eq. 5** and **Eq. 6** are the energy equations for the fluid and the PCM, respectively:

$$\begin{aligned} &\varepsilon_B C_{p,F} \rho_F \left(\frac{\partial T_F}{\partial t} + u_F \nabla T_F \right) = \\ &k_{F,z} \frac{\partial^2 T_F}{\partial z^2} + k_{F,r} \left(\frac{\partial^2 T_F}{\partial r^2} + \frac{1}{r} \frac{\partial T_F}{\partial r} \right) + h_{FPCM} \left(T_{PCM} - T_F \right) - U_{Wext} \left(T_W - T_{ext} \right) \end{aligned} \tag{5}$$

$$(1-\varepsilon_B)\rho_{PCM} \frac{\partial H_{PCM}}{\partial t} = k_{PCM,z} \frac{\partial^2 T_{PCM}}{\partial z^2} + k_{PCM,r} \left(\frac{\partial^2 T_{PCM}}{\partial r^2} + \frac{1}{r} \frac{\partial T_{PCM}}{\partial r} \right) + h_{FPCM} \left(T_F - T_{PCM} \right) \tag{6}$$

In a parametric study, Cheralathan et al., (2006) developed a 1D continuous solid phase model assuming an adiabatic tank and fully developed heat transfer fluid. The authors investigated the influence of Stephan and Stanton numbers, as well the porosity of the bed in the system. A validation of the model was conducted with experimental results.

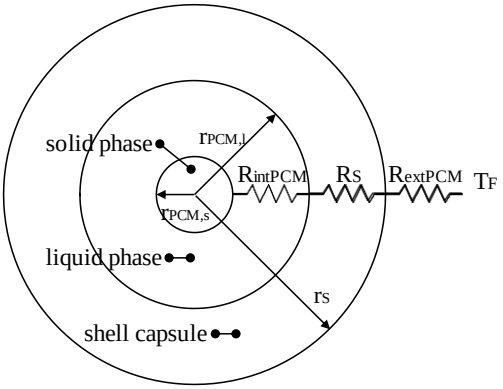

Fig. 6. Thermal resistances assumed in the overall heat coefficient for the PCM.
Source: Adapted from Gracia; Cabeza (2017).

Zanganeh et al., (2014) proposed a multilayer packed bed system for the 1D continuous phase model where the convection heat transfer coefficient was modified to take into account the conduction within the PCM particles. The authors found that the PCM greatly stabilizes the effluent temperature at the discharge, decreasing the temperature drop from sensible heat storage systems.

In a similar work for the 1D phase model, Wu; Fang (2011) incorporated, in the convective coefficient that expresses the PCM-fluid interface, the conductive thermal transfer coefficient of the PCM shell as an effective convective transfer coefficient, where the natural convection of the PCM was neglected. The results were compared with experimental data from literature.

Rady (2009) included an effective thermal conductivity for one dimension. The material fluid fraction and latent heat were viewed as different phases. A parametric investigation was conducted after the model was validated with experimental data. The authors concluded that carefully choosing a mixing ratio of multiple granular phase change components can significantly increase the overall storage system efficiency compared to a PCM with a single granular composite. Ismail; Stuginsky (1999) stress the importance of taking into consideration the effective thermal conductivity to better investigate the heat conduction in the boundary between fluid and solid PCM.

2.13 Concentric dispersion model

This model assumes a thermal gradient in the PCM particles (DE GRACIA; CABEZA, 2017). The axial heat conduction can be added for the PCM and/or the HTF. Thus, the energy

equations can be written for the HTF (**Eq. 7**), the boundary of PCM (**Eq. 8**), and inside the PCM sphere (**Eq. 9**):

$$\varepsilon_B C_{p,F} \rho_F \left(\frac{\partial T_F}{\partial t} + u_F \nabla T_F \right) = \nabla \left(\varepsilon_B k_F \nabla T_F \right) + h_{FPCM} \left(T_{PCM} - T_F \right) - U_{Wext} \left(T_W - T_{ext} \right) \tag{7}$$

$$\begin{aligned} &(1-\varepsilon_B)\rho_{PCM} \frac{\partial H_{PCM}}{\partial t} = \\ &(1-\varepsilon_B)k_{PCM,z} \frac{\partial^2 T_{PCM}}{\partial z^2} + k_{PCM,r} \left(\frac{\partial^2 T_{PCM}}{\partial r^2} + \frac{1}{r} \frac{\partial T_{PCM}}{\partial r} \right) + h_{FPCM} \left(T_F - T_{PCM} \right) \end{aligned} \tag{8}$$

$$\rho_{PCM} \frac{\partial H_{PCM}}{\partial t} = \frac{1}{r^2} \frac{\partial}{\partial r} \left(k_{PCM,z} r^2 \frac{\partial T_{PCM}}{\partial r} \right) \tag{9}$$

A concentric dispersion model proposed by Ismail et al., (2002) discretized the column where in each layer only the fluid transfers energy to the PCM particles. An effective thermal conductivity is used for the natural convection in the molten phase of the PCM. A moving grid method and finite-different approach was used to solve the model, which was validated against the authors' experimental results. The feed temperature, the mass flow in the tank and the temperature of the PCM capsule were studied.

In a similar work to study natural convection inside the PCM particles using the effective thermal conductivity, Wu et al., (2014) also assumed to have axial heat conduction for the fluid and the bed. The authors neglected heat losses to the surroundings and considered that the phase change temperature is constant. It was concluded that the latent heat is around 70% of the total energy storage capacity of the PCM, as a result of the role of the sensible cooling of the HTF and PCM.

To increase the performance of a solar system using air as HTF, Karthikeyan et al. (2014) developed a concentric dispersion model and investigated how different parameters impact the heat transfer rate for both charge and discharge steps. The enthalpy methodology was applied for the phase change. The authors showed that for the system studied, the low convective term is more crucial compared to the thermal conductivity of the PCM since air was used as heat transfer fluid.

2.14 PCM-assisted fixed bed adsorption

One of the strategies applied to maximize the amount of fluid adsorbed per unit time in PSA processes is to use the fast PSA technology, where the time for the total cycle is reduced (CHAI; KOTHARE; SIRCAR, 2011; LOPES; GRANDE; RODRIGUES, 2012), and the most common approach for this method is to increase the bed size (VEMULA; SIRCAR, 2017) thus contributing to creating a near adiabatic system. Hence, the heat of adsorption is crucial in these processes as the adsorption capacity reduces as the temperature increases. In this context, thermal energy storage systems, such as PCM, may be relevant as these materials can act as a heat sink during the adsorption step, and as a heat source for the desorption process.

Using AC as adsorbent, Zimmermann; Keller (2006) experimentally studied the performance of a fixed bed by applying PCMs. The system was loaded with volatile hydrocarbons and the authors investigated the optimum amount of PCM that maximizes the capacity of the bed by varying the ratio of the material in the bed. It was found that 25 wt.% of PCM/AC added to the column increased the amount of gas adsorbed by 15 wt.% in the adsorption step.

Toledo et al., (2013) used an organic material as PCM packed in rubber spheres to study the thermal effect of CO_2 adsorption on both charge and discharge cycles of a fixed bed. A numerical study was conducted and validated experimentally. Both temperature and discharge amount were analyzed experimentally from 8 to 30 bar. The authors found that the central region of the bed endures the most critical temperature variation thus requiring more PCM. The PCM improved the amount of CO_2 adsorbed by 800 L compared to the process without the material.

An organic PCM combining capric and lauric acid was processed by Li; Li, (2015) to study the thermal effect on both charge and discharge steps on a PSA adsorption system for storage of natural gas. The PCM was encapsulated in six copper tubes and distributed uniformly inside the adsorption column. The authors found that by filling the bed with a volume ratio of 6.10% of PCM, the temperature variation can be decreased by 21.8 ºC in the charging step and increased by 22.7 ºC in the discharge step. Moreover, the amount of natural gas delivered was increased by 39.4 vol.% when PCM was added compared to a tank with adsorbents only.

2.15 Mathematical models for PCM-assisted fixed bed adsorption

As discussed before, there are very few researches offering predictive dynamic models for PCM-assisted fixed bed adsorption. The models presented below will be used as reference for this project.

Horstmeier et al. (2016) developed a model integrating PCM with a VSA process. Three adsorbents were used for comparison, i.e., zeolite 13x, AC, and amine. A substantial improvement in efficiency when using the hybrid PCM-adsorbent system. It was also concluded that PCM integrated systems are more important for processes with high heat of adsorption. The authors combined the PCM and adsorbent into one unique particle, whereas the heat balance for the adsorbent was expressed by:

$$\lambda_z\left(\frac{\partial^2 T_A}{\partial r^2}+\frac{2}{r}\frac{\partial T_A}{\partial r}\right)=\rho_A\left[C_{p,A}\frac{\partial T_A}{\partial t}+\sum_i\left(-\Delta H_{ads,i}\right)\frac{\partial q_i}{\partial t}\right] \tag{10}$$

The first term represents the radial dispersion, which has to be taken into account for a single particle PCM-adsorbent, neglecting the axial contribution, where the gas still moves in the axial direction. The last term is the heat released by the adsorbent particles.

For the PCM, an enthalpy balance was assumed:

$$\frac{\partial H_{PCM}}{\partial t}=\frac{U_{PCM}\alpha_{PCM}}{\rho_{PCM}\left(1-\varepsilon_B\right)\varphi_{PCM}}\frac{\partial T_S}{\partial t} \tag{11}$$

Where the variation of enthalpy of the PCM is dependent of the temperature of the copper shell, T_S, which has its own energy balance:

$$\frac{\partial T_S}{\partial t}=\frac{1}{R_S\rho_S C_{p,S}}\left(\frac{\partial^2 T_S}{\partial r^2}+\frac{2}{r}\frac{\partial T_S}{\partial r}\right) \tag{12}$$

The R_S represents the resistance due to conduction of the PCM shell, which will determine the rate of energy is delivered to the PCM.

This model may be interesting for novel processes of PCM integrated with the adsorbent, which requires specific conditions to be applied. Meanwhile, it may not be suitable for cases where

the heat transfer between PCM and adsorbent is not high, or when the PCM is not distributed homogeneously in the bed, where the assumption of unique particle is not valid.

In a recent study, Sakanaka et al., (2020) developed a 1D model for a fixed bed non-isothermal adsorption with AC and paraffin wax as PCM. An experimental setup measuring the breakthrough curve for n-butane was used to validate the model. The melting temperature and the fraction of PCM was investigated to evaluate adiabatic adsorption performance. With the results, the authors proposed a simple heat conservation equation for the ideal weight fraction of PCMs that maximize the sorbent loading during the charging step.

The authors considered a 1D model with thermal equilibrium between the gas phase, adsorbent and PCM shell:

$$\begin{aligned}&\left[\varepsilon_B\sum_i c_i C_{p,G}+\rho_B\left(1-\varphi_{PCM}\right)C_{p,A}+\rho_B\varphi_{PCM}\left(1-\theta_{PCM}\right)C_{p,S}+\rho_B\left(1-\varphi_{PCM}\right)\sum_i q_i C_{p,G}\right]\frac{\partial T_B}{\partial t}\\&-\varepsilon_B\frac{\partial P}{\partial t}=-\sum_i\left(u_G c_i-\varepsilon_B D_z\frac{\partial c_i}{\partial z}\right)C_{p,G}\frac{\partial T_B}{\partial t}+\rho_B\left(1-\varphi_{PCM}\right)\left(-\Delta H_{ads,i}\right)\frac{\partial q_i}{\partial t}+\\&\varepsilon_B\lambda_z\frac{\partial^2 T_B}{\partial z^2}+\rho_B\varphi_{PCM}U_{PCM}\left(T_{PCM}-T_B\right)+\frac{4}{d_{W\,\mathrm{int}}}h_{GW}\left(T_W-T_B\right)\end{aligned}\qquad(13)$$

where θ_{PCM} represents the PCM fraction compared to PCM shell.

The simplification of pseudo-homogeneous model can be a good approximation when the shell is a strong conductor, which was considered in the balance as a source term ($\rho_B\varphi_{PCM}\left(1-\theta_{PCM}\right)C_{p,S}$) for temperature change in the bed. The PCM will act as a heat sink with a convection term ($\rho_B\varphi_{PCM}U_{PCM}\left(T_{PCM}-T_B\right)$) analogous to the loss to the ambient. The conduction inside the PCM was neglected and a similar approach will be used in this project, except it will not be a pseudo-homogeneous model. When the PCM volume fraction, φ_{PCM} is zero, then the expression is reduced to the well-known pseudo-homogeneous model for adsorption. An enthalpy balance was conducted for PCM in the same way as shown in **Eq. 11**.

As it was pointed out, an optimum volume fraction of PCM is required to maximize the sorbate loading, since the integration of PCM in the adsorption system inevitably lowers the adsorbent amount in the bed. Furthermore, it was observed that there are not many papers

emphasizing the numerical models for PCM-adsorbent integrated systems, which is the focus of this manuscript.

2.16 Selecting the PCM for fixed beds

When choosing a phase change material for fixed bed adsorption, three important parameters are (WU, Shaofei et al., 2020) the (i) temperature of phase change to satisfy the practical application, a temperature of phase change slightly above the initial temperature of the system is required; (ii) the latent heat of the material should provide high heat storage capacity; (iii) the thermal conductivity should be high. The latter is not attainable for most PCMs (DE GRACIA; CABEZA, 2017).

Toledo et al., (2013) used an organic PCM with a phase change temperature of 22 ºC. The initial temperature of the system was 15 ºC. The paraffin applied as PCM by Sakanaka et al. (2020) had a melting point 2 ºC above the system initial temperature. The authors highlighted that one advantage in using paraffin is that the melting temperature can be easily modified by modifying the paraffin structure, making them suitable for a range of applications in the context of gas separation by adsorption.

3 Mathematical model for a fixed bed PCM-assisted adsorption process

Fig. 7 shows the schematic diagram of the system that has been investigated, with cylindrical encapsulated PCM elements filling a cylindrical adsorption tank. The tank is fed with a N_2-CO_2 gas mixture at constant flow rate. The CO_2 is preferentially adsorbed in the bed, so a gas stream of nearly pure N_2 leaves the bed. The bed temperature changes with position and time due to the heat of adsorption and heat loss to the environment. The process is ideally interrupted at the breakthrough point, when the N_2 gas starts to be contaminated with CO_2.

A model was developed in which the PCM acts as heat sink for the adsorption process, based on fundamental conservation equations of mass, momentum and energy for the gas, the adsorbent and the PCM, coupled to kinetics of adsorption and to heat transfer between the fluid, the adsorbent and the PCM. In analogy with Shumann´s model, heat transfer was assumed to occur only by convection. The lack of an equation describing the dispersion inside the PCM can lead to an underestimation of the heat transfer dynamics, hence an overall heat transfer coefficient between the packed bed and PCM was introduced to simulate the heat exchange mechanisms. This approach is similar to the one developed by a Sakanaka et al., (2020), with the addition of the overall heat transfer coefficient U_{PCM} described in the section “Schumann's model”. The authors also used a pseudo-homogeneous model, e.g., it was assumed thermal equilibrium between gas and adsorbent, whereas in this work there are different heat equations describing the gas and adsorbent energy conservation (heterogenous model).

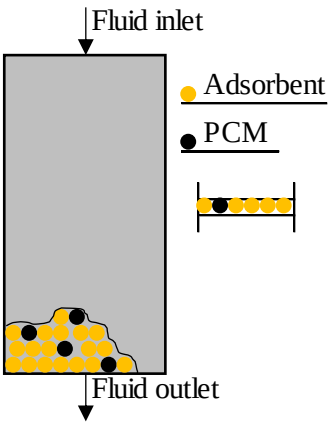

Fig. 7. Simplified layout of the fixed bed system with PCM and adsorbent uniformly distributed in the column.

The key dependent variables for the conservation of energy are: temperature of gas phase (T_G), adsorbent (T_A), PCM (T_{PCM}), and wall (T_W). The main variable for the conservation of mass is the concentration of the gas phase (c_i). The variable related to the rate of adsorption is q_i.

The correlations used for estimation of mass and heat parameters and physical and transport properties can be found in Item 3.5.

The main assumptions are:

1. 1D model (no radial dispersion);
2. Axial dispersion for the flow in the tank;
3. PCM axial heat conduction neglected (Schuman's model);
4. Heat transfer between gas and adsorbent was taken into account;
5. Heat transfer between gas and PCM was considered;
6. Heat transfer between PCM and adsorbent was neglected;
7. Adsorbent-fluid equilibrium described by the Toth isotherm;
8. Mass transfer rate between fluid and adsorbent described by the linear driving force (LDF) model;
9. Ideal gas;
10. Constant column void fraction;
11. Homogeneous adsorbent properties;
12. Pressure drop in the bed is neglected;
13. PCM evenly and randomly distributed in the bed.

3.1 Adsorbent

The Toth isotherm is useful to describe the adsorption of CO_2/N_2 on AC and zeolites (DANTAS, Tirzhá L.P.; LUNA; SILVA; TORRES; et al., 2011):

$$q_{eq} = q_m \frac{K_{eq} p}{\left[1+\left(K_{eq} p\right)^{\chi}\right]^{1/\chi}} \tag{14}$$

The adsorbate concentration in equilibrium, q_{eq}, is function of the fluid temperature, which can change substantially in processes involving gas separation. The simplest expression to describe

the isotherm's temperature dependence for isosteric heat of adsorption is the van't Hoff equation (RUTHVEN; XU, 1993):

$$K_{eq} = K_{eq0} \exp\left(\frac{-\Delta H_{ads}}{RT_G}\right) \tag{15}$$

The adsorption equilibrium will be more favorable to a specific gas depending on its affinity with the adsorbent. CO_2 is preferentially adsorbed in comparison to N_2 for both AC and zeolite 13x (SAMANTA et al., 2012).

3.2 Dynamic model

The local fluid temperature varies within the MTZ, so a heat dispersion with coefficient λ_z is considered. The dispersion component compiles a number of heat transfer mechanisms, such as natural convection, conduction, and even radiation, thus usually referred as an effective axial thermal conductivity.

The axial superficial velocity will change with time due to decline of adsorbate concentration in a bulk separation system, except for very low feed adsorbate concentration systems, more common in purification processes (GUTIÉRREZ ORTIZ; BARRAGÁN RODRÍGUEZ; YANG, 2019).

The energy conservation equations for the fluid and adsorbent (heterogeneous model) can be written as (DANTAS, Tirzhá L.P.; LUNA; SILVA; TORRES; et al., 2011; RUTHVEN; XU, 1993; WU, Shaofei et al., 2020):

$$\begin{aligned}&\varepsilon_B CC_{v,G} \frac{\partial T_G}{\partial t} + \nabla\left(-\varepsilon_B \lambda_z \nabla T_G\right) + CC_{p,G} \nabla u_G T_G = \\ &-\left(1-\varepsilon_B\right)\frac{6h_{GA}}{d_A}\left(T_G - T_A\right) - \frac{1}{1-\varphi_{PCM}}\frac{\alpha_{PCM}}{1-\varepsilon_B}U_{PCM}\left(T_G - T_{PCM}\right) - \frac{4h_{GW}}{\varepsilon_B d_{W\,\mathrm{int}}}\left(T_G - T_W\right)\end{aligned} \tag{16}$$

$$\rho_A C_{p,A} \frac{\partial T_A}{\partial t} = \frac{6h_{GA}}{d_A}\left(T_G - T_A\right) + \rho_A \sum_i \left(-\Delta H_{ads,i}\right)\frac{\partial q_i}{\partial t} \tag{17}$$

In the left side of **Eq. 16** the sum of the rate of enthalpy's change for the gas, the axial dispersion of the fluid and the net enthalpy related to the fluid flow in the control volume is represented. The first term on the right side represents the heat transfer by convection between gas

and adsorbent. The second is the convection heat exchange between the fluid and the PCM (Schuman's model). The third term reflects the heat loss for the column's wall.

In **Eq. 17**, the left side represents the rate of enthalpy change of the adsorbent in the control volume. The first term on the right side reflects the heat exchange by convection between the adsorbent and the fluid. It is assumed that the adsorbent does not exchange heat with the PCM. The last term is the heat generated by the adsorption.

The term α_{PCM} represents the ratio between the cross-sectional area of PCM shell (A_S) and the column volume (V_C):

$$\alpha_{PCM} = \frac{A_S}{V_C} \tag{18}$$

The PCM energy conservation equation depends whether the PCM is a solid below its melting temperature, a solid in equilibrium with a liquid, or a liquid above its melting temperature. In the fixed bed process, three steps may be distinguished. The first step (**Eq. 19**) is for the solid state, where the PCM stored sensible heat until the material begins to melt. In the second step, the PCM absorbs a large amount of energy as the material changes the state from solid to liquid (**Eq. 20**). In the third stage, the PCM completely melts and the energy is stored again as sensible heat, but in liquid phase (**Eq. 21**) (GAO et al., 2021).

$$\left(1-\varepsilon_B\right)\rho_{PCM,s}C_{p,PCM,s}\frac{\partial T_{PCM}}{\partial t} = U_{PCM}\alpha_{PCM}\left(T_G - T_{PCM}\right) \tag{19}$$

$$\left(1-\varepsilon_B\right)\rho_{PCM,s}\frac{\partial H_{PCM}\omega_{PCM}}{\partial t} = U_{PCM}\alpha_{PCM}\left(T_G - T_{PCM}\right) \tag{20}$$

$$\left(1-\varepsilon_B\right)\rho_{PCM,l}C_{p,PCM,l}\frac{\partial T_{PCM}}{\partial t} = U_{PCM}\alpha_{PCM}\left(T_G - T_{PCM}\right) \tag{21}$$

Even though the energy balance of PCM does not consider the contribution of the PCM shell and the temperature gradient inside the material particles, U_{PCM} (**Eq. 4**) estimates the thermal resistance for the capsule shell and the PCM solid-liquid film layer during phase change. If U_{PCM} is large enough, the rate of heat transfer between gas and PCM will be sufficiently high to restrain the temperature rise of the bed thus strengthening the adsorption capacity of the adsorbent. One recognizable and easy way to obtain parameters for the PCM is by evaluation the resistance due

to conduction of the capsule shell, which has to be low for a more effective U_{PCM}. A capsule shell with high thermal conductivity, like copper or aluminum, and a small thickness, are better suited in this application.

For the column wall, the energy balance can be written as (DANTAS, Tirzhá L.P.; LUNA; SILVA; TORRES; et al., 2011):

$$\rho_W C_{p,W} \frac{\partial T_W}{\partial t} = \alpha_W h_{GW} \left(T_G - T_W\right) - \alpha_{Wl} U_{Wext} \left(T_W - T_{ext}\right) \tag{22}$$

To describe an adiabatic process, the environmental loss must be neglected, i.e., $U_{Wext} \rightarrow 0$.

The mass balance for each species "*i*" in the gas phase, with a common axial mass dispersion coefficient D_z, can be expressed by (HELFFERICH, 1985):

$$\varepsilon_B \frac{\partial c_i}{\partial t} + \nabla\left(-\varepsilon_B D_z \nabla c_i\right) + \nabla u_G c_i = -\rho_A \left(1-\varepsilon_B\right) \frac{\partial q_i}{\partial t} \tag{23}$$

With the mass transfer rate defined by the well-known linear driving force model (HORSTMEIER; GOMEZ LOPEZ; AGAR, 2016)

$$\frac{\partial q_i}{\partial t} = k_{LDF,i} \left(q_{eq,i} - q_i\right) \tag{24}$$

where $K_{LDF,i}$ (s^{-1}) defines the rate of adsorption for species "*i*".

The concentration c_i for an ideal gas is given by:

$$c_i = \frac{y_i P}{R T_G} \tag{25}$$

The pressure drop was evaluated using the Ergun equation (RAY; DAS, 2020).

3.3 Boundary conditions

Constraining the composition to fixed values at an inlet to a packed bed reactor may lead to issues with physically inconsistent high adsorption rates or singularities at the inflow boundary conditions (BC). These obstacles can be reduced by using a flux BC, based on the upstream concentrations and the fluid velocity at the boundary. The usual BC applied to solve a system of

second order PDE in separation adsorption processes are the Robin-type or Danckwerts-type for the inlet fluid flow, which are also known as flux-source type BC. They specify inflow conditions for domains where large adsorption rates are predicted in the proximity to the inlet (DANCKWERTS, 1953).

The flux-source BC was applied for inflow ($z = 0$):

$$\left(u_G c_i\right)_{z^-} = -\varepsilon_B D_z \left(\nabla c_i\right)_{z^+} + \left(u_G c_i\right)_{z^+} \tag{26}$$

$$\left(u_G CC_{p,G}\right)_{z^-} = -\varepsilon_B \lambda_z \left(\nabla T_G\right)_{z^+} + \left(u_G CC_{p,G}\right)_{z^+} \tag{27}$$

$$\left(u_G C\right)_{z^-} = \left(u_G C\right)_{z^+} \tag{28}$$

$$\left(\nabla T_W\right)_{z^-} = 0 \tag{29}$$

Note that the dispersion coefficient for both conservation of mass (D_z) and energy (λ_z) appeared, which is required for Robin-type BC. The subscripts z^- and z^+ denote, respectively, the point just before and after entering (for inlet) or exiting (for outlet) the packed bed, thus a continuity of flux is asserted since the concentration at entrance will be limited by the gas diffusion.

At the outflow, no adsorption happens, since there are no adsorbent particles hence no variation in gas concentration. However, considering the axial dispersion, it leads to an incoherent system due to an unrecognized outlet temperature or concentration. This problem is mitigated by imposing a steady concentration at the outlet BC, which is done by forcing a homogeneous Neumann outflow BC (CHENG, A. H.-D.; CHENG, 2005). Coppola; Levan, (1981) demonstrated that these BC can be applicable for steady fluid-phase concentration and the flux at the outflow for packed bed adsorption systems even with axial dispersion playing an important role in the downstream.

The Neumann BC was applied for outflow ($z = L_W$):

$$\left(\nabla c_i\right)_{z^-} = 0 \tag{30}$$

$$\left(\nabla T_G\right)_{z^-} = \left(\nabla T_W\right)_{z^-} = 0 \tag{31}$$

3.4 Fixed bed design

Simulations were carried out for flue gas with a CO_2 molar fraction of 0.2 flowing in a cylindrical adsorption tank of 3.1 cm radius and 40 cm length filled with adsorbent and macroencapsulated PCM with a copper shell of thickness equal to 0.1 mm and 39 cm length randomly distributed in the bed and oriented along the column axis.

The adsorption step was conducted at different pressures until the bed reached thermal equilibrium with the environment. The range of parameters and a detailed list of the properties will be given and discussed later in the Results and discussion section.

3.5 Correlations

The use of correlations is crucial to modelling and the prediction of the fixed-bed dynamics. Nonetheless, there are a great number of correlations and they have to be carefully selected according to the process specification.

These correlations are often expressed as function of dimensionless such as Reynolds, Schmidt, Peclet, Nusselt or Rayleigh. Ortiz; et al., (2019) detailed each correlation with their respective constraints and literature reference.

Dimensionless numbers (DANTAS, Tirzhá L.P.; LUNA; SILVA; DE AZEVEDO; et al., 2011; GUTIÉRREZ ORTIZ; BARRAGÁN RODRÍGUEZ; YANG, 2019)*:*

Reynolds number:

$$\mathrm{Re} = \frac{\rho_G u_G d_A}{\mu_G} \tag{32}$$

Schmidt number:

$$Sc = \frac{\mu_G}{\rho_G D_m} \tag{33}$$

Peclet number:

$$Pe = \frac{u_G d_A}{D_z} \tag{34}$$

Prandtl number:

$$\mathrm{Pr} = \frac{C_{p,G} u_G}{k_G} \tag{35}$$

Rayleigh number:

$$Ra = g\beta \frac{\left(T_W - T_{ext}\right)}{\nu_{ext} \alpha_{ext}} \tag{36}$$

Estimation of model parameters correlations (DANTAS, Tirzhá L.P.; LUNA; SILVA; DE AZEVEDO; et al., 2011)*:*

Bosanquet equation:

$$\frac{1}{D_z} = \tau \left(\frac{1}{D_m} + \frac{1}{D_K} \right) \tag{37}$$

Knudsen:

$$D_K = 9700 r_{pore} \left(\frac{T_G}{M_i} \right)^{1/2} \tag{38}$$

Axial mass dispersion:

$$\varepsilon_B \frac{D_z}{D_m} = 20 + \frac{1}{2} Sc \,\mathrm{Re} \tag{39}$$

Film mass transfer:

$$Sh = 2 + 1.1 \mathrm{Re}^{0.27} \, Sc^{1/3} \tag{40}$$

Axial heat dispersion:

$$\frac{\lambda_z}{k_G} = 10 + \frac{1}{2} \mathrm{Pr}\,\mathrm{Re} \tag{41}$$

Film heat transfer:

$$Nu = 2 + 1.1 \mathrm{Pr}^{1/3} \, \mathrm{Re}^{3/5} \tag{42}$$

Internal convective heat coefficient:

$$\frac{1}{k_G} = \frac{1}{h_{GW} d_{W\,\mathrm{int}}} \left(\frac{25}{2} + 0.048\,\mathrm{Re} \right) \tag{43}$$

Global heat transfer coefficient:

$$\frac{1}{U_{Wext}} = \frac{1}{h_{GW}} + \frac{d_{W\,\mathrm{int}}}{k_W} \ln\left(\frac{d_{Wext}}{d_{W\,\mathrm{int}}} \right) + \frac{d_{W\,\mathrm{int}}}{d_{Wext}} \frac{1}{h_{ext}} \tag{44}$$

External convective heat transfer coefficient:

$$\frac{h_{ext} L_W}{k_{ext}} = 0.68 + \frac{0.67 Ra^{1/4}}{\left[1 + \left(0.492/\mathrm{Pr} \right)^{3/4} \right]^{4/9}} \tag{45}$$

4 Model validation

The model just described was implemented using MATLAB® and COMSOL Multiphysics®. Spatial discretization was done by the Finite Element Method and the time integration used the Backward Differentiation Formulas method. The Damped Newton Method was used to ensure convergence. The model code can be found on Appendix I.

To validate the model, experimental data was extracted from literature (DANTAS et al., 2011; SIQUEIRA et al., 2018). The two case studies were for CO_2 separation from a mixture of CO_2/N_2. The data used in simulations was the same as the ones from reference; the isotherms used in the original contributions were fitted to a Toth isotherm, which was used in the present model.

4.1 Case study 1. CO_2 and N_2 separation on activated carbon (MAGALHÃES SIQUEIRA et al., 2018)

Siqueira et al., (2018) study CO_2 capture in post-combustion adsorption. **Table 1** shows the operational conditions, physical and transport properties of the proposed process.

Table 1. Data of the case study 1 (SIQUEIRA et al., 2018).

Data	Parameter	Description	Value
Adsorbent	ρ_A	density of the adsorbent particles	471 kg m^{-3}
	d_A	diameter of the adsorbent particles	3.5 mm
Bed	ε_B	porosity of the bed	0.41
	d_{Wint}	bed internal diameter	2.8 cm
	L_W	total length of the bed	54.9 cm
Operation	P_{in}	operating pressure	6 bar; 12 bar
	T_{ext}	fluid temperature at the bed inlet	298 K
	$y_{CO2,in}$	volume fraction of CO_2 at the bed inlet	0.1
	F_{in}	fluid flow-rate at the bed inlet	6.65 L min^{-1}
Isotherm	$K_{eq0,CO2}$	equilibrium constant of the isotherm for CO_2	$\left[1.379\cdot10^{-9}\exp\left(1881/T_G\right)\right]$ [Pa^{-1}]
	$q_{m,CO2}$	saturation charge of the adsorbent for CO_2	$\left(23.051-0.0347T_G\right)$ [mol kg^{-1}]
	$\Delta H_{ads,CO2}$	enthalpy of adsorption for CO_2	-17341 J mol^{-1}
	$K_{eq0,N2}$	equilibrium constant of the isotherm for N_2	$\left[4.155\cdot10^{-9}\exp\left(729/T_G\right)\right]$ [Pa^{-1}]
	$q_{m,N2}$	saturation charge of the adsorbent for N_2	$\left(10.116-0.0199T_G\right)$ [mol kg^{-1}]
	$\Delta H_{ads,N2}$	enthalpy of adsorption for N_2	-12201 J mol^{-1}
Wall	$C_{p,W}$	column wall specific heat	477 J kg^{-1} K^{-1}
	ρ_W	column wall density	786 kg m^{-3}

Additional parameters were calculated using the correlations presented in Item 3.5. The inflow gas is composed of CO_2 and N_2 1:9 molar. AC (Norit RB4) is used as adsorbent

Fig. 8 shows the temperature history and breakthrough curve obtained by the researchers (points), and the simulations of the presented model (solid lines). The numerical simulation represented well the experimental data. The discrepancies in the breakthrough curve presented in **Fig. 8c** is due to the simple isotherm equation used in the simulation, which take place sooner than the experimental data, hence may lead to a slight underestimation of the amount of gas adsorbed.

a) 6 bar **b) 12 bar**

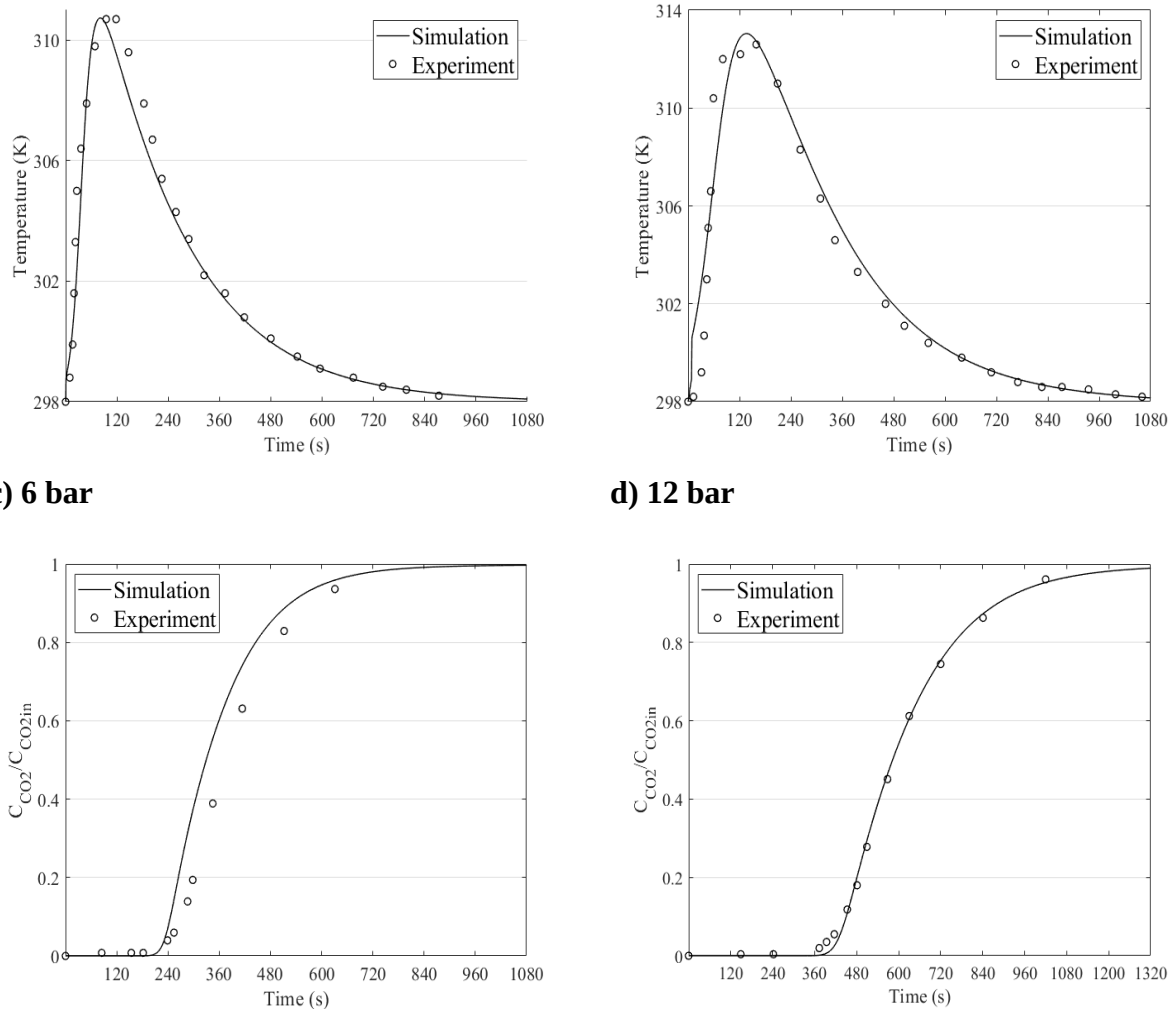

c) 6 bar **d) 12 bar**

Fig. 8. Temperature history and breakthrough curve for case study 1 (MAGALHÃES SIQUEIRA et al., 2018).

The temperature history was based on a distance of 0.15 m of the bed inlet. The uptake at the beginning of numerical simulation of the temperature curve (**Fig. 8a** and **Fig. 8b**) is due to the dead volume in the experimental setup, which was not taken into account in the simulations. Since in this space only gas expansion occurs and no adsorption takes place, then no major differences can be seen in the global shape of the curve.

Even though pressures above 10 bar were conducted, the use of ideal gas still is plausible and the numerical simulation had good agreement with the experimental data at 12 bar, since the density of the gas is not severely impacted by the pressure. Moreover, the dispersion plays an important role in the breakthrough and temperature curves and other parameters like the physical properties of the gas may be important but not decisive for the complex adsorption phenomena, entering the effective dispersion coefficient for both mass and temperature conservations.

The maximum temperature is higher for the 12 bar adsorption (**Fig. 8b**) in comparison to 6 bar (**Fig. 8a**). This is because the amount of gas in equilibrium with adsorbent increases as the pressure increases, leading to a rise of heat released during the adsorption step. Moreover, the breakthrough time is higher for 12 bar (**Fig. 8d**), since the mass transfer zone develops slower as the adsorption capacity increases.

4.2 Case study 2. CO_2 and N_2 separation on zeolite 13x (DANTAS, T. L. P et al., 2011)

The behavior of a nitrogen-saturated fixed-bed adsorption of carbon dioxide-nitrogen mixture on zeolite 13x was studied by Dantas et al. (2011). A thermocouple was placed at 1/5 from the inlet of an 83.1 cm length column. The experimental data extracted from the reference is shown in **Table 2**. Additional parameters were calculated using the correlations presented in Item 3.5.

Fig. 9 shows the temperature history and breakthrough curve obtained by the researchers (points), and the simulations of the presented model (solid lines). The numerical simulation had good agreement with experimental data. The mathematical model slightly underestimated the environmental loss, which can be attributed to the prediction of the overall heat transfer coefficient between bed wall and environment by the correlations. This can happen for cases where, for example, the wall thickness is too small or the conduction in the wall is high enough to be represented by a constant coefficient (U_{Wext}) rather than a source term involving heat dispersion in the column wall. Despite this, during the adsorption, both temperature and breakthrough curve of

the numerical solution aligned well with experimental data, thus this loss is not as important as the isosteric heat released when the mass transfer zone is still active.

It's critical to notice the difference between the temperature rise in Case study 1 (**Fig. 8a** and **Fig. 8b**) and Case study 2 (**Fig. 9a**). For the first, which used AC as adsorbent, the gas temperature increased 12.7 ºC and 15 ºC for operating pressures of 6 bar and 12 bar, respectively; while in Case study 2, this temperature rise was of 40 ºC to only 1.2 bar, where zeolite 13x was applied. The disparity is due to zeolites having a greater adsorption capacity compared to AC, and this behavior is reflected in the isosteric heat of adsorption, which in this case the parameter for the zeolite material is almost twice as big (29.4 kJ mol^{-1} *vs.* 17.3 kJ mol^{-1} for AC), promoting a sharper increase in temperature for the gas, even for lower pressures. The fact that zeolites can operate in pressures close to 1.0 bar may be useful for applications where lower pressures are required, as in post-combustion CO_2 technologies.

Table 2. Data of the case study 2 (DANTAS et al., 2011).

Data	Parameter	Description	Value
Adsorbent	ρ_A	density of the adsorbent particles	1228.5 kg m^{-3}
	ε_A	porosity of the adsorbent particles	0.37
	d_A	diameter of the adsorbent particles	2.9 mm
Bed	ε_B	porosity of the bed	0.41
	d_{Wint}	bed internal diameter	2.1 cm
	L_W	total length of the bed	83.1 cm
Operation	P_{in}	operating pressure	1.2 bar
	T_{ext}	fluid temperature at the bed inlet	306 K
	$y_{CO2,in}$	volume fraction of CO_2 at the bed inlet	0.1
	F_{in}	fluid flow-rate at the bed inlet	$3.5 \cdot 10^{-5}$ m^3 s^{-1}
Isotherm	$K_{eq0,CO2}$	equilibrium constant of the isotherm for CO_2	$4.31 \cdot 10^{-4}$ bar^{-1}
	$q_{m,CO2}$	saturation charge of the adsorbent for CO_2	5.09 mol kg^{-1}
	$\Delta H_{ads,CO2}$	enthalpy of adsorption for CO_2	-29380 J mol^{-1}
	$K_{eq0,N2}$	equilibrium constant of the isotherm for N_2	$8.81 \cdot 10^{-5}$ bar^{-1}
	$q_{m,N2}$	saturation charge of the adsorbent for N_2	3.08 mol kg^{-1}
	$\Delta H_{ads,N2}$	enthalpy of adsorption for N_2	-17190 J mol^{-1}
Wall	l_W	column wall thickness	0.41 cm
	$C_{p,W}$	column wall specific heat	500 J kg^{-1} K^{-1}
	k_W	column wall conductivity	13.4 W m^{-1} K^{-1}
	ρ_W	column wall density	8238 kg m^{-3}

As the adsorbate is strongly attached to zeolite surface, high amount of energy for bed regeneration is required (YANG, R. T., 2003), thus a complete energetic and/or exergetic analysis of the process for both adsorption and desorption steps, as well the maximum number of charging cycles, have to be investigated.

The breakthrough curve, shown in **Fig. 9b**, had a sharp slope, and therefore the MTZ for this adsorbent is stable, hence less adsorbate is lost in the outlet as the breakthrough point and exhaustion point (**Fig. 4**) are closer to each other, making it easier to determine the saturation time for the adsorption step.

a) **b)**

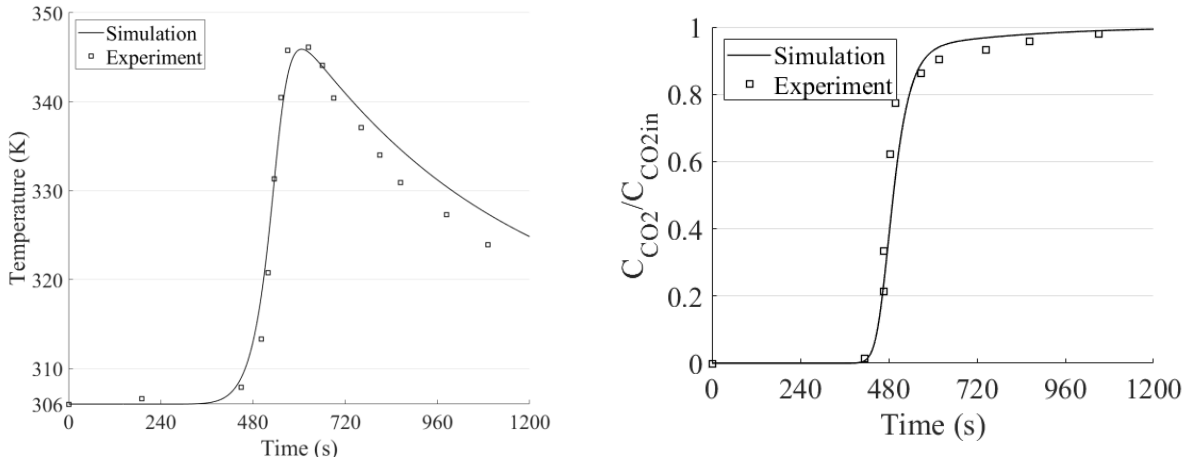

Fig. 9. Temperature history and breakthrough curve for case study 2 (DANTAS, T. L. P et al., 2011).

5 Results and discussion

For adsorption separation, adsorption capacity and bed capacity are two commonly used performance parameters. For PCM assisted adsorption the latter is more convenient because it takes into account the bed temperature. Research involving PCM assisted fixed bed adsorption broadly use the total amount of gas adsorbed as a bed performance framework, usually in volume of total fluid adsorbed at standard temperature and pressure (STP) per volume of column volume. A typical curve is the bed capacity (calculated in the breakthrough point) in the y-axis *versus* the volume fraction of the phase change material in the column in the x-axis (BELLAN et al., 2015; HORSTMEIER; GOMEZ LOPEZ; AGAR, 2016; MOTA, 2008; PRADO et al., 2021; SAKANAKA et al., 2020; TOLEDO et al., 2013).

The fixed bed analysis was done for both AC and zeolite 13x. Even though zeolite 13x has larger heat of adsorption, AC requires lower energy for regeneration. Therefore, the numerical investigation is focused on AC, and the zeolite 13x is proposed as a possible successor as more research is done optimizing the adsorbent.

5.1 Numerical analysis and simulation conditions

It was found that the numerical simulations are independent of space-element and time step size below 8 mm and 1 s, respectively, hence these values were chosen in all calculations.

The process conditions and fixed bed geometry are, as discussed in Item 3.4, presented in **Table 3**. The parameters for the adsorbents and PCM were taken from literature and can be found in **Table 3** with their respective references.

The bed capacity is the main aspect for performance evaluation. Key parameters of the analysis are the effect of PCM volumetric fraction in the bed, the radius of the capsule, the flow rate of the working fluid, and the inlet temperature of the fluid. In **Table 4** is shown the range of operating parameters.

At the start of operation, the bed is assumed to be in equilibrium with pure nitrogen at given temperature and pressure, that is, $C_{N2} = P_{in}/(RT_{in})$ and $q_{N2} = q_{N2,sat}$. The initial conditions are given in **Table 5**.

Table 3. Process specification.

Parameter	Description	Value
	Bed	
ε_B	porosity of the bed	0.52
d_{Wint}	bed internal diameter	6.17 cm
L_W	total length of the bed	40.0 cm
	Activated carbon (AC) (DANTAS, Tirzhá L.P.; LUNA; SILVA; DE AZEVEDO; et al., 2011)	
ρ_A	density of the adsorbent particles	1138 kg m^{-3}
ε_A	porosity of the adsorbent particles	0.46
d_A	diameter of the adsorbent particles	3.8 mm
$C_{p,A}$	adsorbent heat capacity	880 J kg^{-1} K^{-1}
	AC isotherm (DANTAS, Tirzhá L.P.; LUNA; SILVA; DE AZEVEDO; et al., 2011)	
$K_{eq0,CO2}$	equilibrium constant of the isotherm for CO_2	$7.62 \cdot 10^{-5}$ bar^{-1}
$q_{m,CO2}$	saturation charge of the adsorbent for CO_2	10.05 mol kg^{-1}
$\Delta H_{ads,CO2}$	enthalpy of adsorption for CO_2	-21840 J mol^{-1}
$K_{eq0,N2}$	equilibrium constant of the isotherm for N_2	$6.91 \cdot 10^{-5}$ bar^{-1}
$q_{m,N2}$	saturation charge of the adsorbent for N_2	9.74 mol kg^{-1}
$\Delta H_{ads,N2}$	enthalpy of adsorption for N_2	-16310 J mol^{-1}
	Zeolite 13x (DANTAS, T. L. P et al., 2011)	
ρ_A	density of the adsorbent particles	1228.5 kg m^{-3}
ε_A	porosity of the adsorbent particles	0.41
d_A	diameter of the adsorbent particles	2.1 mm
$C_{p,A}$	adsorbent heat capacity	920 J kg^{-1} K^{-1}
	13x isotherm (DANTAS, T. L. P et al., 2011)	
$K_{eq0,CO2}$	equilibrium constant of the isotherm for CO_2	$4.31 \cdot 10^{-4}$ bar^{-1}
$q_{m,CO2}$	saturation charge of the adsorbent for CO_2	5.09 mol kg^{-1}
$\Delta H_{ads,CO2}$	enthalpy of adsorption for CO_2	-29380 J mol^{-1}
$K_{eq0,N2}$	equilibrium constant of the isotherm for N_2	$8.81 \cdot 10^{-5}$ bar^{-1}
$q_{m,N2}$	saturation charge of the adsorbent for N_2	3.08 mol kg^{-1}
$\Delta H_{ads,N2}$	enthalpy of adsorption for N_2	-17190 J mol^{-1}
	PCM (paraffin wax) (SAKANAKA et al., 2020)	
T_{mPCM}	PCM melting point	27 ºC
ΔH_{PCM}	latent heat of PCM paraffin wax	$2.45 \cdot 10^5$ J kg^{-1}
ρ_{PCM}	PCM density	880 kg m^{-3}
$C_{p,PCM,s}$	PCM heat capacity (solid phase)	1800 J kg^{-1} K^{-1}
$C_{p,PCM,l}$	PCM heat capacity (liquid phase)	2100 J kg^{-1} K^{-1}
	Wall (DANTAS, Tirzhá L.P.; LUNA; SILVA; DE AZEVEDO; et al., 2011)	
l_W	column wall thickness	4.1 mm
$C_{p,W}$	column wall specific heat	500 J kg^{-1} K^{-1}
ρ_W	column wall density	8238 kg m^{-3}

Table 4. Range of operating parameters.

Parameter	Description (unit)	Value range
$V_{f,PCM}$	PCM volume fraction in the column (%v/v)	0
		1
		2
		3
$d_{PCM,int}$	PCM internal diameter (mm)	1,0
		2,0
		3,0
$u_{G,in}$ ($F_{G,in}$)	gas superficial velocity (gas inlet flow rate)	0.56 cm/s (1 L/min)
		1.67 cm/s (3 L/min)
T_{in}	fluid inlet temperature (ºC)	20
		25

5.2 Effect of PCM volume fraction in the bed

This item presents the base case. Keeping the inlet pressure constant at 6 bar and the superficial velocity (inflow rate) of 0.56 cm/s (1 L/min), for variable number of paraffin PCM devices of cylindrical shape with a length of L_{PCM} = 39 cm and a diameter of $d_{PCM,int}$ = 2 mm, the time evolution of the gas and PCM temperature at the middle of the bed, i.e., at $z = L_W/2$ was obtained for AC with T_{in} = 25 ºC. In **Fig. 10a** is shown that the temperature of the gas in the absence of PCM increases by more than 16 °C due to the release of the heat of adsorption. Since adsorption is an exothermic process, the equilibrium term, K_{eq}, reduces when the gas temperature increases hence the bed capacity decreases.

Table 5. Initial conditions.

Parameter	Description	Value
T_G	Gas temperature	T_{in}
T_A	Adsorbent temperature	T_{in}
T_{PCM}	PCM temperature	T_{in}
T_W	Wall temperature	T_{in}
T_{ext}	External temperature	T_{in}
$y_{CO2,in}$	CO_2 inlet volume fraction	0.2
$P_{in,AC}$	Inlet pressure for AC	6 bar
$P_{in,13x}$	Inlet pressure for zeolite 13x	1.2 bar
$C_{CO2,in}$	CO_2 inlet concentration	0
$C_{N2,in}$	N_2 inlet concentration	$\frac{P_{in}}{RT_{in}}$
q_{CO2}(z,0)	amount adsorbed of CO_2 in $t = 0$	0
q_{N2}(z,0)	amount adsorbed of N_2 in $t = 0$	q_{sat}

Moreover, the axial dispersion coefficient, D_z, increases with temperature, considering that it corresponds directly with the diffusivity, which is proportional to the 1.75th times the temperature. Consequently, the slope of the breakthrough decreases, and the bed saturation time will be reached earlier. In other words, the MTZ expands and the bed capacity decreases.

The heat evolved in the adsorption is directly linked to the breakthrough curve. The heat liberated over time reaches a peak at any bed segment, that directly correlates to the maximum inclination of the breakthrough curve. The gas temperature rises and subsequently decreases (**Fig. 10a**), reaching a maximum reciprocal to the maximum value of the rate $\partial q_i/\partial t$, and the surroundings cool afterwards. Heat is exchanged from the bed (adsorbent) to the fluid. The fluid heats the adsorbent downstream the MTZ, which has not contributed so far in the adsorption process and, thus, it still at initial temperature.

The pattern of temperature profiles leans on the axial thermal conductivity, λ_z. As follows, if no axial thermal conductivity was taken into account, the temperature peak would be higher, since the amplitude of the MTZ would contract, and the adsorption would happen in a narrower region of packed-bed. A higher inflow concentration would likewise lead to a higher temperature, as the amount of gas adsorbed per time at any MTZ segment would be larger.

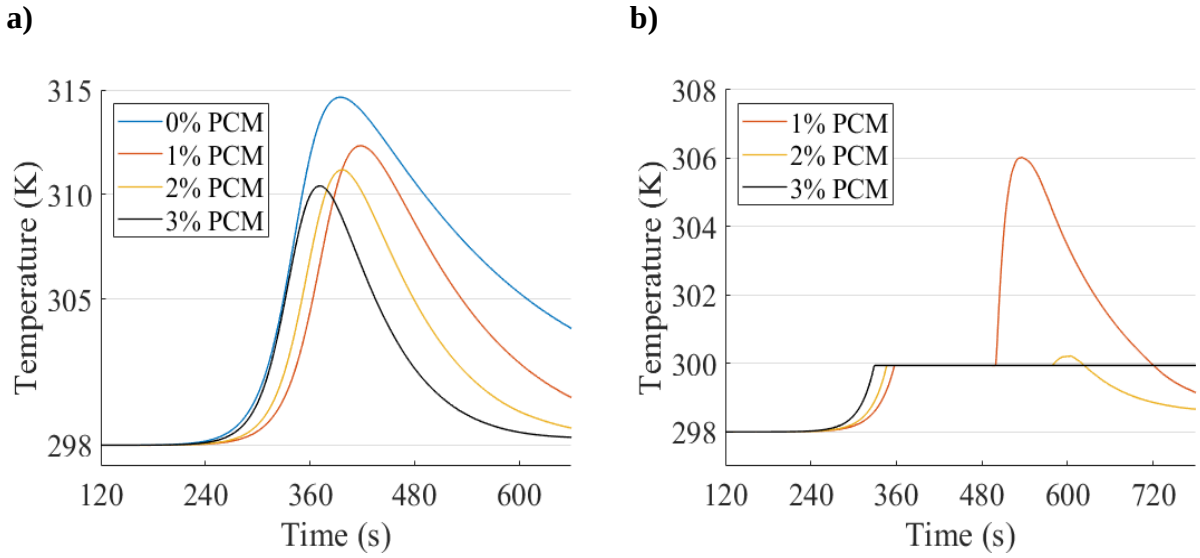

Fig. 10. Temperature history at $z = L_W/2$ of the a) Gas and the b) PCM.

By adding small amounts of PCM, the temperature increment decreases. For 1% of PCM added, it decreases the maximum temperature reached by the gas by 2 ºC (**Fig. 10a**) and increases the amount of gas adsorbed in the bed by up to 10.7% in volume of CO_2 (**Fig. 11a**).

Fig. 10b shows that when 1% PCM is added, all of the PCM melts, but the temperature continues to rise, so valuable bed space is wasted. With 2% PCM, most of the PCM melts, which is desirable. However, melting takes place too late in comparison with the breakthrough time, so again not all of the PCM potential is used. Increasing the amount of PCM even more to 3% has the same effect as 2%, and part of the PCM does not even melt, it only occupies valuable space that would be otherwise filled with adsorbent. Consequently, as shown in **Fig. 11a**, the bed capacity is maximal at 1% of PCM added, as the gain in equilibrium capacity for the adsorbent more than compensates the adsorbent removed from the column.

The slope of the breakthrough curve (**Fig. 11b**) increases directly with PCM added, which can be useful for purification and separation systems since the length of unused bed decreases.

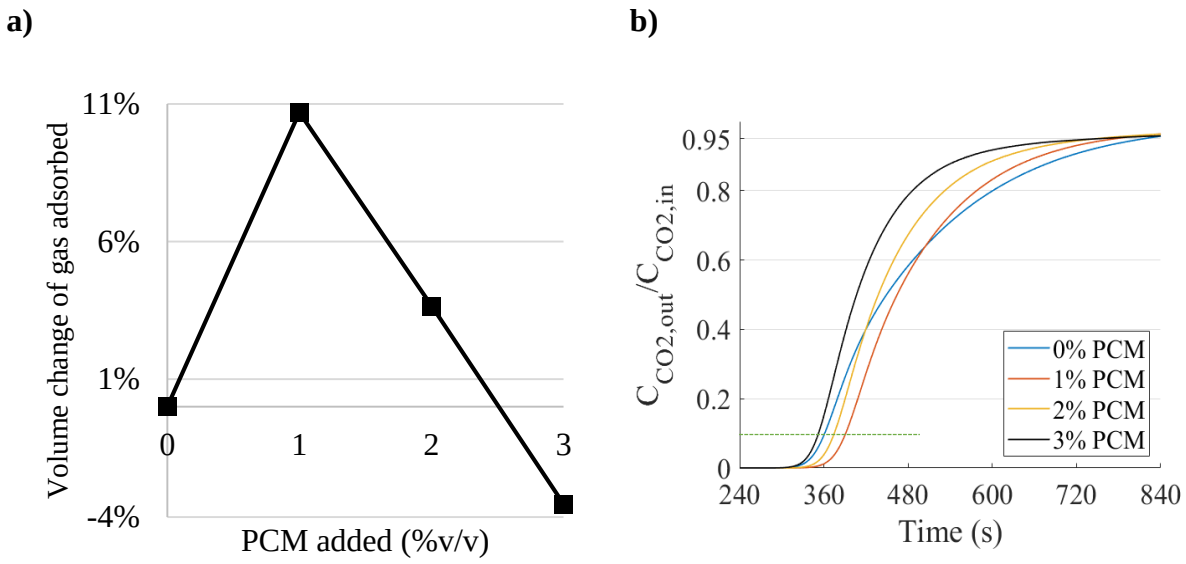

Fig. 11. (a) Volume of gas increased when PCM is added and (b) breakthrough curve for the adsorption step.

5.3 PCM heat transfer interval (HTI)

To better understand why the amount of gas adsorbed reaches a maximum for a certain fraction of PCM added and to provide a guideline parameter for the design of PCMs, the concepts of “PCM heat transfer interval” (HTI) and “PCM effective heat transfer interval” (EHTI) were proposed. The HTI represents time interval of the process in which the PCM changes phase (melts or crystallizes). The first point of the EHTI is when the PCM starts melting (thus are the same for HTI and EHTI) and the last point is when the MTZ reaches almost complete saturation, say 90%. As the PCM can store more energy with the material latent heat, the HTI should be slightly higher than the EHTI to provide the maximum bed capacity.

For the system analyzed in the previous subsection, **Fig. 12** shows that for 1% of PCM results for HTI and EHTI that are well suited in restricting the temperature increase of the bed. Above 1% of PCM added, as shown in **Fig. 13**, the HTI is too large hence the latent heat of this material stops acting, because most of the adsorption has already occurred while only part of the PCM melted, leaving its region of effective heat transfer interval (EHTI). When increasing the amount of PCM, the higher the positive difference between the HTI and EHTI, the less effective the PCM becomes. Therefore, the EHTI and HTI can be used as useful parameters in the design of PCM.

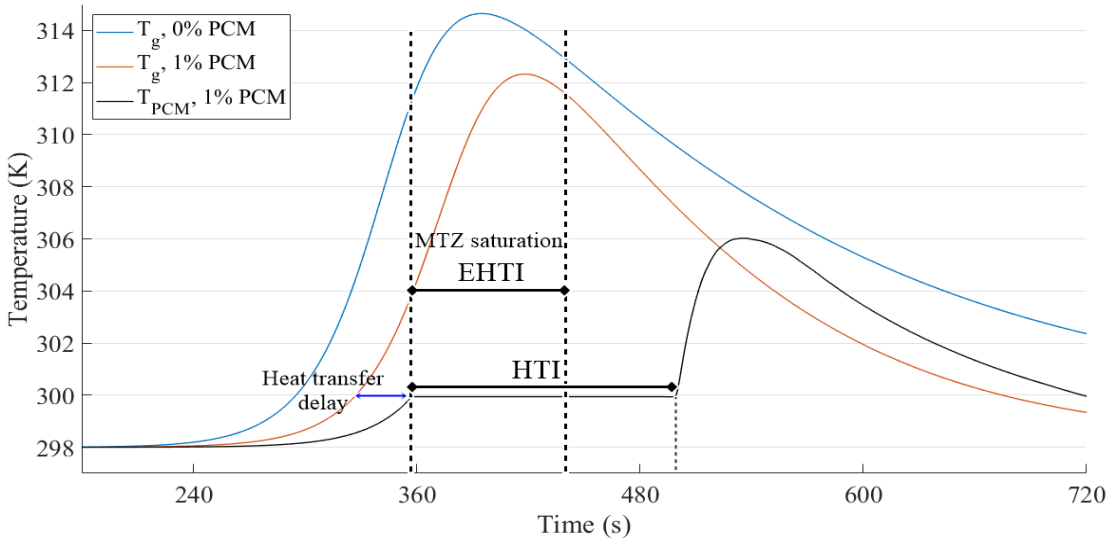

Fig. 12. Heat transfer interval (HTI) represents the interval where the PCM is melting and the effective heat transfer interval (EHTI) reflects the interval where the PCM is melting before the bed reaches complete breakthrough.

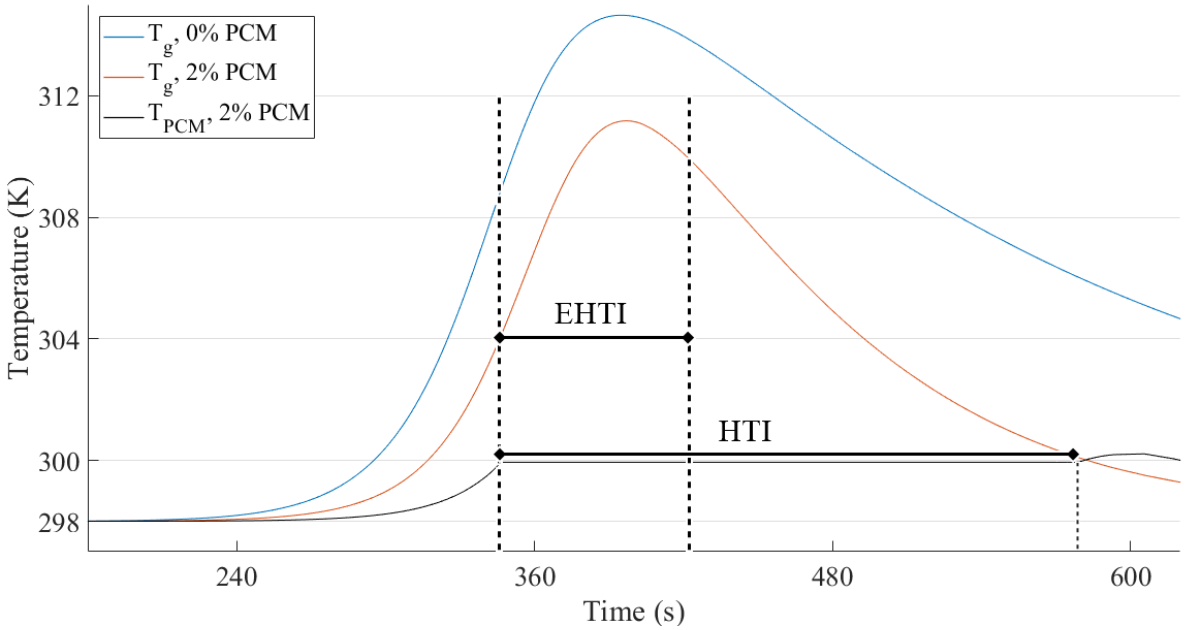

Fig. 13. HTI and EHTI for 2%v/v of PCM, which is larger than the 1% PCM HTI.

5.4 Effect of PCM device size

Three PCM capsules with diameters of 1, 2 and 3 mm were compared, considering 1%, 2% and 3 vol.% PCM in the bed, keeping the other parameters of the system as the base case. **Fig. 14** shows the gas and PCM temperatures for 1% PCM added and **Fig. 15** shows the bed capacities. As expected, for the same volume fraction of PCM in the bed, the heat transfer happens more slowly as the PCM diameter is increased. In general, by increasing the PCM diameter, the larger the HTI is. In principle the match between EHTI and HTI increases as the diameter decreases, so it would be expected that the bed capacity increases for smaller diameters. This trend was confirmed as 2 mm was better than 3 mm (**Fig. 15**). However, the 1 mm PCM yielded a lower capacity. This was attributed to the metallic shell, which occupies a large proportion of the PCM element for such small diameter.

Devices of all diameters tested did not melt completely at 3% of PCM added to the bed. Besides, the PCM with 3 mm diameter did not melt entirely with only 2% PCM added, as its area of heat transfer with the gas was smaller compared to the other materials device sizes, and the sensible heat of the material is not as effective as its latent heat storage capacity. Moreover, for the 1 mm capsule, as the shell thickness is the same for all capsule diameters, the dead volume (volume of the copper shell) lead to a wasted space higher than the 2 mm capsule.

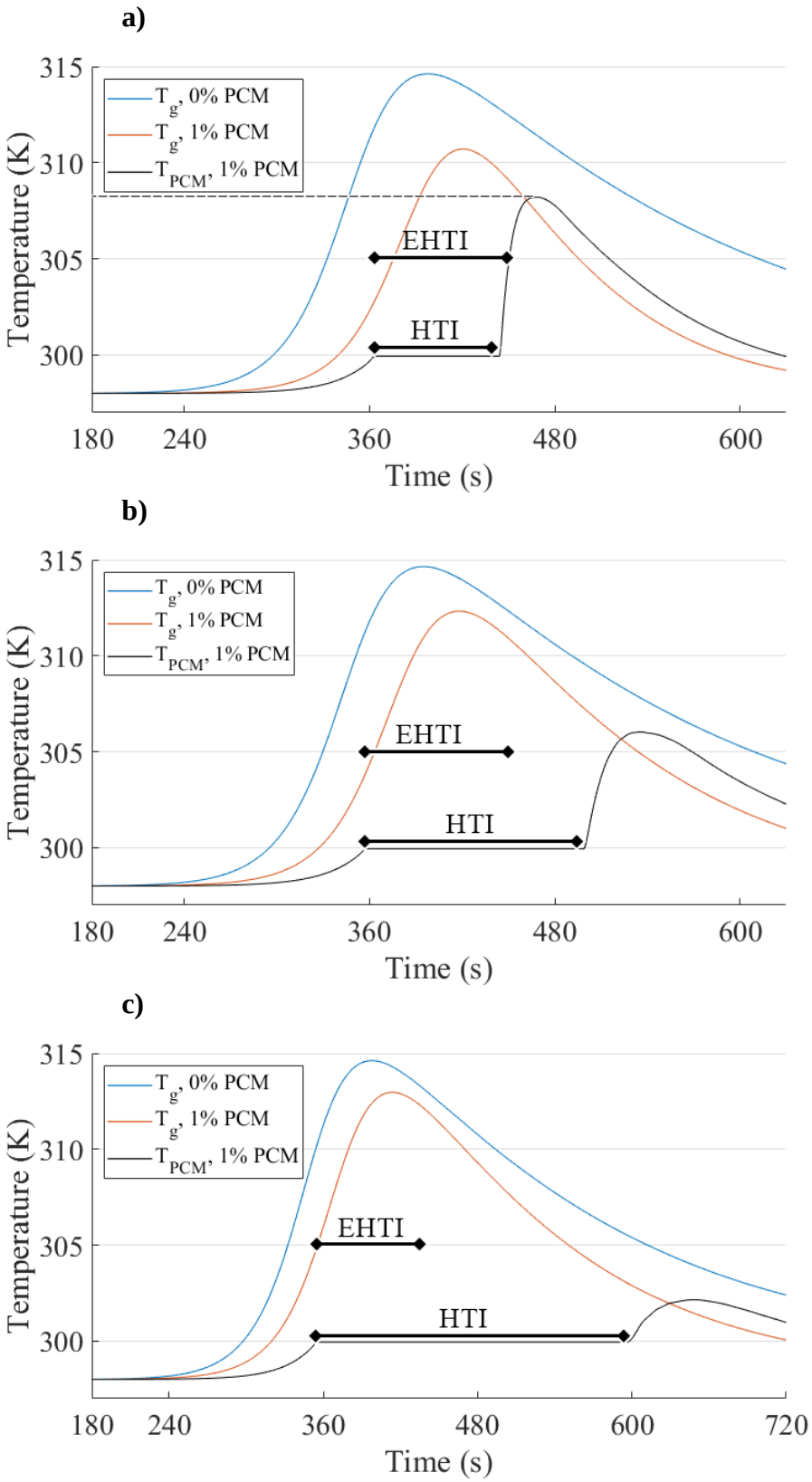

Fig. 14. Temperature history at $z = L_W/2$ for a) 1 mm, b) 2 mm, and c) 3 mm PCM internal diameter.

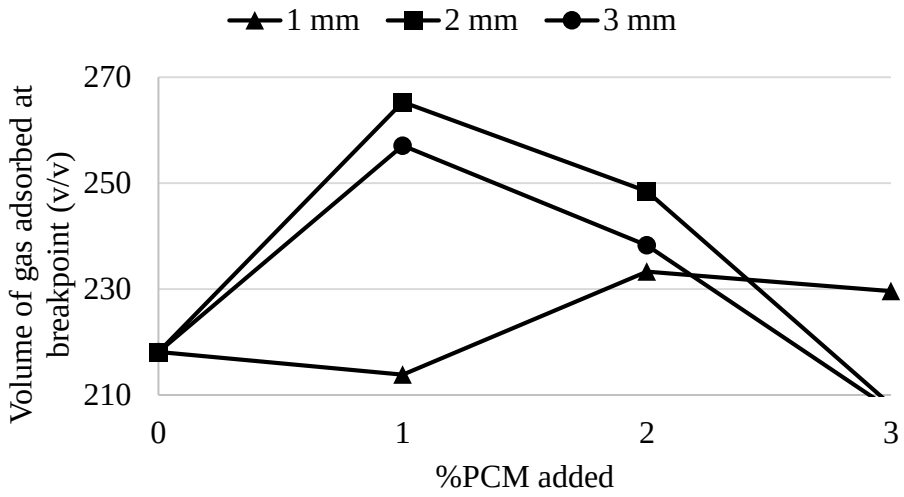

Fig. 15. Comparison of amount of bed capacity for different PCM device size.

Fig. 15 also shows, when 2 mm and 3 mm PCM elements are considered, there is an optimum amount of PCM to be added because of the competing effects of latent-heat delivery (desirable) and bed volume space occupied by the PCM (undesirable). Besides, excessive PCM may lead to incomplete PCM melting (undesirable).

5.5 Effect of gas velocity (inlet flow rate)

As shown in **Fig. 16a**, the rate of adsorption was much faster when increasing the superficial velocity (flow rate) from 0.56 cm/s (1 L/min) to 1.67 cm/s (3 L/min), and the time to reach the gas temperature peak was reduced by almost 120 seconds. For a superficial velocity of 1.67 cm/s, the PCM did not improve the amount of gas adsorbed in none of the range of operating parameters (**Table 4**). since the material could not effectively store energy in such a small time, as exemplified in **Fig. 16b** for a PCM with a diameter of 2 mm. This knowledge is important because the superficial velocity can limit the use of PCM as heat sink in these processes. A probable cause is that the PCM melts too late, after the bed breakthrough time. A possible solution would be to design microencapsulated PCM to increase the heat exchange rate.

5.6 Effect of inlet temperature

As discussed before, the temperature of the system has to be aligned with the melting temperature of the PCM as the sensible heat of these materials cannot store energy as latent heat

does. When decreasing the inlet temperature to 20 ºC, i.e., 7 ºC distant from the melting point of the PCM, in none of the simulations within the range of operating parameters (**Table 4**) the PCM provided a greater amount of gas adsorbed, as the PCM did not melt completely, and the EHTI was far from the HTI.

The PCM system still provided a decrease of gas temperature in the bed as more PCM was added, but it was more due to adsorbent removal rather than the PCM acting as a heat sink for the process.

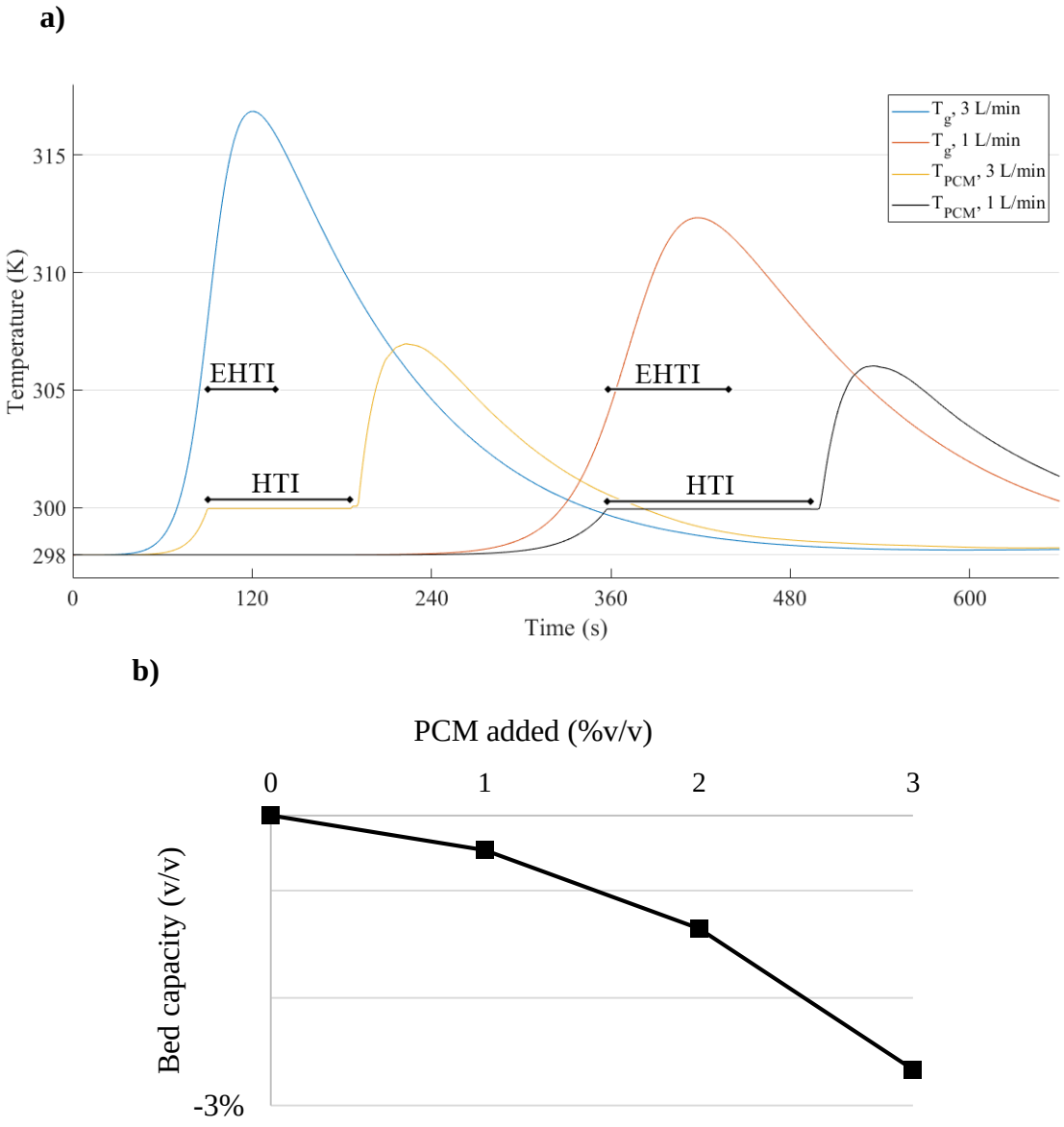

Fig. 16. (a) Temperature history at $z = L_W/2$ and 1% of PCM added for 0.56 cm/s (1 L/min) and 1.67 cm/s (3 L/min) and (b) Volume of CO_2 adsorbed decreased when PCM is added to a 1.67 cm/s system.

5.7 Effect of PCM according to axial position

For 1 vol.% PCM device of diameter of $d_{PCM,int}$ = 2 mm, the profile of the difference between the peak gas temperature for a bed with and without PCM (ΔT_G), according to the axial direction was obtained in **Fig. 17**.

Each MTZ has its own HTI. From the beginning to half of the bed, the PCM heated and melted, but after the middle of the column, the gas temperature increase is almost equal to the case without PCM. This phenomenon happens because the breakthrough curve (**Fig. 11b**) does not have a sharp slope, thus the MTZ is behind the ideal case (**Fig. 18**), therefore the phase change material may be better placed outside downstream part of the bed. This behavior was also found by **Regin *et al.* (2009)** (FELIX REGIN; SOLANKI; SAINI, 2009), where the PCM progressively lost its effectiveness after half of the bed and did not melt near the column exit.

5.8 Effect of PCM on zeolite 13x

- T_{in} = 25 ºC. F_{in} = 1 L/min. L_{PCM} = 39 cm. $d_{PCM,int}$ = 2 mm. %PCM = variable.

Fig. 19a shows the total amount of gas adsorbed for AC and zeolite 13x. The inlet pressure for zeolite was 1.2 bar, lower than the 6 bar applied for AC and the zeolite 13x was capable of adsorbing almost 30% more in volume of gas compared to the AC in the absence of PCM. The PCM decreased the maximum global temperature reached by the gas in 5 ºC when 2% of PCM was added, promoting an increase of 12.7% in total volume of gas adsorbed (**Fig. 19b**).

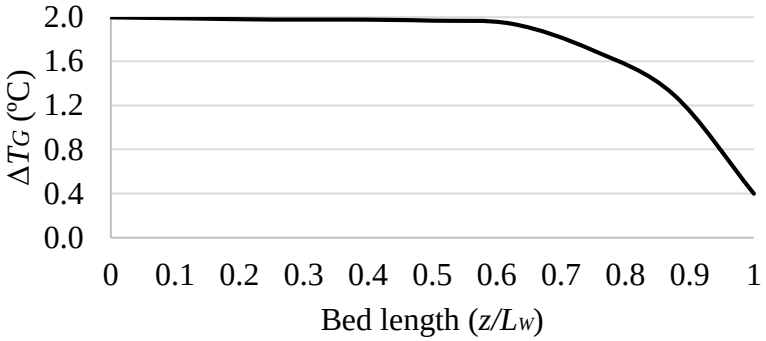

Fig. 17. Maximum gas temperature increase profile.

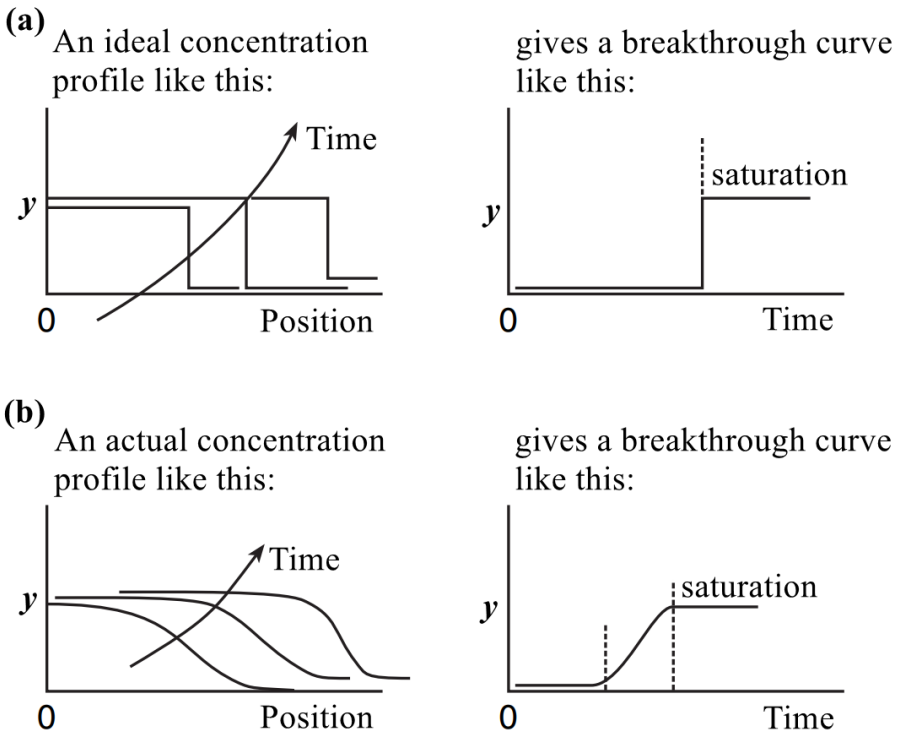

Fig. 18. Breakthrough curves. The abrupt step in (a) is less common than the soft slope in (b). Source: Adapted from Cussler (2009)**.**

For the range of operating parameters, the PCM was more effective for the zeolite 13x compared to the systems with AC, as the heat released during the adsorption strongly decreases the adsorption capacity and therefore the use of a passive heat exchanger prevented the gas loading loss.

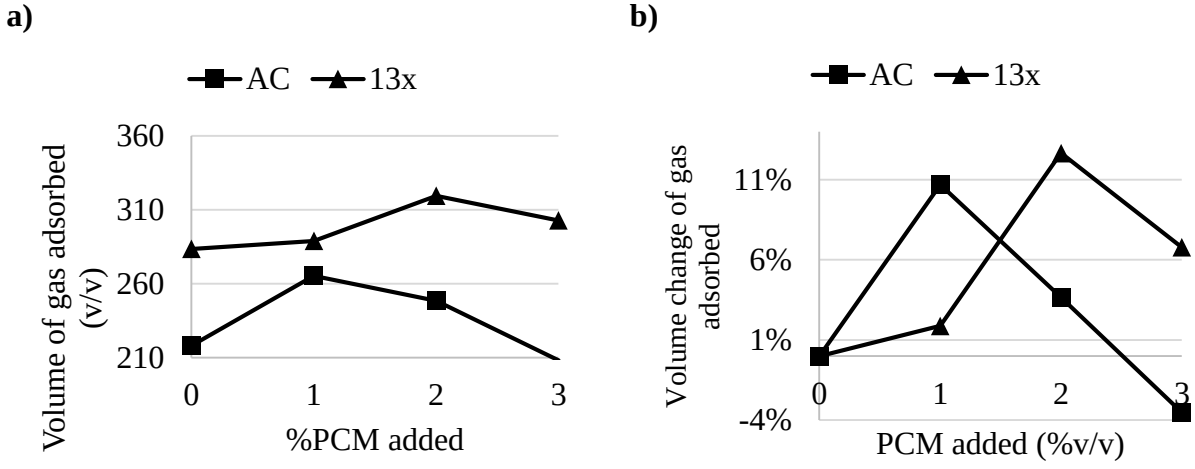

Fig. 19. Comparison of volume change of gas adsorbed for AC and zeolite 13x.

6 Conclusions

The new concepts of heat transfer interval (HTI) and effective heat transfer interval (EHTI) were introduced for the design of PCM-assisted fixed-bed adsorption. The first represents the interval where the PCM melts and the latter reflects the interval where the PCM melts before the MTZ/bed reaches complete breakthrough. To be most efficient, the PCM EHTI and HTI region have to align, besides the PCM should melt fully before the breakthrough time. For the process, a 2 mm diameter PCM was more efficient.

Theoretical studies revealed that the use of PCM increases the bed capacity by 10% in volume of gas for AC, due to the reduction of the maximum temperature of the process by 2 ºC, for 1% of volume of PCM added. Compared to the 6 bar fixed bed AC process investigated, the PCM adapted slightly better to the zeolite 13x system, providing 12.7% in volume of gas adsorbed to only 2 vol.% of PCM added to column at a lower pressure of 1.2 bar. This happened because zeolites release more heat of adsorption compared to activated carbon. Combining phase change materials in zeolite 13x PSA and TSA technologies may contribute to improve bed capacity in the adsorption and desorption cycles.

The gas velocity can limit the effectiveness of the material in storing heat, and it may not be suitable in processes that require fast adsorption, requiring the design of microencapsulated PCM. In contrast of systems with a gas velocity of 0.56 cm/s, when the gas velocity is 1.67 cm/s, the PCM did not provide larger amount of adsorbed gas.

When the inflow temperature was 2 ºC lower than the PCM melting point. For an inflow temperature 7 ºC lower than the PCM melting point, not all of the PCM melted and the sensible heat alone did not increase the bed capacity.

The PCM did not melt entirely after a certain point of the bed, and thus it may be adequate to place the PCM outside downstream part of the bed for systems where the breakthrough curve does not have a sharp slope.

References

ACKLEY, M. W.; YANG, R. T. Kinetic separation by pressure swing adsorption: Method of characteristics model. **AIChE Journal**, v. 36, n. 8, p. 1229-1238, Aug. 1990. DOI 10.1002/aic.690360812.

AMIN, N. A. M.; BELUSKO, M.; BRUNO, F. An effectiveness-NTU model of a packed bed PCM thermal storage system. **Applied Energy**, v. 134, p. 356-362, Dec. 2014. DOI 10.1016/j.apenergy.2014.08.020.

ARORA, S.; POTŮČEK, F. Modelling of displacement washing of packed bed of fibers. **Brazilian Journal of Chemical Engineering**, v. 26, n. 2, p. 385-393, June 2009. DOI 10.1590/S0104-66322009000200016.

BASTOS-NETO, M.; AZEVEDO, D. C. S.; LUCENA, S. M. P. **Adsorption**. Kirk-Othmer Encycl. Chem. Technol. [S.l.]: Wiley, 2020. 59 p.

BASUMATARY, R. et al. Thermal modeling of activated carbon based adsorptive natural gas storage system. **Carbon**, v. 43, n. 3, p. 541-549, Aug. 2005. DOI 10.1016/j.carbon.2004.10.016.

BELLAN, S. et al. Numerical and experimental studies on heat transfer characteristics of thermal energy storage system packed with molten salt PCM capsules. **Applied Thermal Engineering**, v. 90, p. 970-979, Nov. 2015. DOI 10.1016/j.applthermaleng.2015.07.056.

BEN-MANSOUR, R. et al. Carbon capture by physical adsorption: materials, experimental investigations and numerical modeling and simulations - a review. **Applied Energy**, v. 161, p. 225-255, Jan. 2016. DOI 10.1016/j.apenergy.2015.10.011.

BILOÉ, S.; GOETZ, V.; GUILLOT, A. Optimal design of an activated carbon for an adsorbed natural gas storage system. **Carbon**, v. 40, n. 8, p. 1295-1308, July 2002. DOI 10.1016/S0008-6223(01)00287-1.

BLAZEK, C. P. P. et al. Charge/discharge characteristics of high-capacity methane adsorption storage systems. 1990, [S.l.]: Institute of Electrical and Electronics Engineers, Aug. 1990. p. 306-314. DOI 10.1109/IECEC.1990.716507.

CASINI, M. **Phase-change materials**. Smart Build. [S.l.]: Elsevier, 2016. 218 p.

CHAI, S. W.; KOTHARE, M. V.; SIRCAR, S. Rapid pressure swing adsorption for reduction of bed size factor of a medical oxygen concentrator. **Industrial & Engineering Chemistry Research**, v. 50, n. 14, p. 8703-8710, July 2011. DOI 10.1021/ie2005093.

CHENG, A. H.-D.; CHENG, D. T. Heritage and early history of the boundary element method. **Engineering Analysis with Boundary Elements**, v. 29, n. 3, p. 268-302, Mar. 2005. DOI 10.1016/j.enganabound.2004.12.001.

CHENG, X.; ZHAI, X.; WANG, R. Thermal performance analysis of a packed bed cold storage unit using composite PCM capsules for high temperature solar cooling application. **Applied Thermal Engineering**, v. 100, p. 247-255, May 2016. DOI 10.1016/j.applthermaleng.2016.02.036.

CHERALATHAN, M.; VELRAJ, R.; RENGANARAYANAN, S. Heat transfer and parametric studies of an encapsulated phase change material based cool thermal energy storage system. **Journal of Zhejiang University-SCIENCE A**, v. 7, n. 11, p. 1886-1895, Nov. 2006. DOI 10.1631/jzus.2006.A1886.

CHO, K.; CHOI, S. H. Thermal characteristics of paraffin in a spherical capsule during freezing and melting processes. **International Journal of Heat and Mass Transfer**, v. 43, n. 17, p. 3183-3196, Sept. 2000. DOI 10.1016/S0017-9310(99)00329-4.

CHOI, J. et al. Theoretical evaluation of an organic phase change material (pcm)-inserted dual-functional adsorbent for the recovery of heat of adsorption. **Industrial & Engineering Chemistry Research**, v. 58, n. 23, p. 10114-10118, June 2019. DOI 10.1021/acs.iecr.9b00198.

CHUE, K. T. et al. Comparison of activated carbon and zeolite 13x for CO2 recovery from flue gas by pressure swing adsorption. **Industrial & Engineering Chemistry Research**, v. 34, n. 2, p. 591-598, Feb. 1995. DOI 10.1021/ie00041a020.

CLAUSSE, M.; BONJOUR, J.; MEUNIER, F. Adsorption of gas mixtures in TSA adsorbers under various heat removal conditions. **Chemical Engineering Science**, v. 59, n. 17, p. 3657-3670, Sept. 2004. DOI 10.1016/j.ces.2004.05.027.

COPPOLA, A. P.; LEVAN, M. D. Adsorption with axial diffusion in deep beds. **Chemical Engineering Science**, v. 36, n. 6, p. 967-971, Aug. 1981. DOI 10.1016/0009-2509(81)80081-4.

CUSSLER, E. L. **Diffusion**: mass transfer in fluid systems. 3. ed. [S.l.]: Cambridge University Press, 2009. 606 p.

DANCKWERTS, P. V. Continuous flow systems. **Chemical Engineering Science**, v. 2, n. 1, p. 1-13, Feb. 1953. DOI 10.1016/0009-2509(53)80001-1.

DANTAS, T. L. P et al. Modeling of the fixed - bed adsorption of carbon dioxide and a carbon dioxide - nitrogen mixture on zeolite 13X. **Brazilian Journal of Chemical Engineering**, v. 28, n. 3, p. 533-544, Sept. 2011. DOI 10.1590/S0104-66322011000300018.

DANTAS, Tirzhá L.P.; LUNA, F. M. T.; SILVA, I. J.; TORRES, A. E. B.; et al. Carbon dioxide-nitrogen separation through pressure swing adsorption. **Chemical Engineering Journal**, v. 172, n. 2-3, p. 698-704, May 2011. DOI 10.1016/j.cej.2010.08.026.

DANTAS, Tirzhá L.P.; LUNA, F. M. T.; SILVA, I. J.; DE AZEVEDO, D. C. S.; et al. Carbon dioxide-nitrogen separation through adsorption on activated carbon in a fixed bed. **Chemical Engineering Journal**, v. 169, n. 1-3, p. 11-19, Nov. 2011. DOI 10.1016/j.cej.2011.06.037.

DE GRACIA, A.; CABEZA, L. F. Numerical simulation of a PCM packed bed system: a review.

Renewable and Sustainable Energy Reviews, v. 69, n. p. 1055-1063, Oct. 2017. DOI 10.1016/j.rser.2016.09.092.

DONOHUE, M. D.; ARANOVICH, G. L. Adsorption hysteresis in porous solids. **Journal of Colloid and Interface Science**, v. 205, n. 1, p. 121-130, Sept. 1998. DOI 10.1006/jcis.1998.5639.

ERKEY, C.; TÜRK, M. Thermodynamics and kinetics of adsorption of metal complexes on surfaces from supercritical solutions. **Supercritical Fluid Science and Technology**. p. 73-127, Sept. 2021. DOI 10.1016/B978-0-444-64089-5.00047-0.

FARID, M. M. et al. A review on phase change energy storage: materials and applications. **Energy Conversion and Management**, v. 45, n. 9-10, p. 1597-1615, June 2004. DOI 10.1016/j.enconman.2003.09.015.

FELIX REGIN, A.; SOLANKI, S. C. C.; SAINI, J. S. S. An analysis of a packed bed latent heat thermal energy storage system using PCM capsules: Numerical investigation. **Renewable Energy**, v. 34, n. 7, p. 1765-1773, July 2009. DOI 10.1016/j.renene.2008.12.012.

GAO, L. et al. Parametric analysis of a packed bed thermal storage device with phase change material capsules in a solar heating system application. **Building Simulation**, v. 14, n. 3, p. 523-533, July 2021. DOI 10.1007/s12273-020-0686-2.

GAWANDE, S. M.; BELWALKAR, N. S.; MANE, A. A. Adsorption and its isotherm - theory. **International Journal of Engineering Research**, v. 6, n. 6, p. 312, June 2017. DOI 10.5958/2319-6890.2017.00026.5.

GIELEN, D. et al. The role of renewable energy in the global energy transformation. **Energy Strategy Reviews**, v. 24, p. 38-50, Apr. 2019. DOI 10.1016/j.esr.2019.01.006.

GUTIÉRREZ ORTIZ, F. J.; BARRAGÁN RODRÍGUEZ, M.; YANG, R. T. Modeling of fixed-bed columns for gas physical adsorption. **Chemical Engineering Journal**, v. 378, p. 121985, Dec. 2019. DOI 10.1016/j.cej.2019.121985.

HAGHPANAH, R. et al. Multiobjective optimization of a four-step adsorption process for postcombustion CO2 capture via finite volume simulation. **Industrial & Engineering Chemistry Research**, v. 52, n. 11, p. 4249-4265, Mar. 2013. DOI 10.1021/ie302658y.

HELFFERICH, F. G. Principles of adsorption & adsorption processes, by D. M. Ruthven, John Wiley & Sons, 1984, xxiv + 433 pp. **AIChE Journal**, v. 31, n. 3, p. 523-524, Mar. 1985. DOI 10.1002/aic.690310335.

HORSTMEIER, J. F. F.; GOMEZ LOPEZ, A.; AGAR, D. W. W. Performance improvement of vacuum swing adsorption processes for CO2 removal with integrated phase change material. **International Journal of Greenhouse Gas Control**, v. 47, p. 364-375, Apr. 2016. DOI 10.1016/j.ijggc.2016.02.013.

ISMAIL, K. A. R. A. R. et al. Numerical and experimental study of spherical capsules packed bed latent heat storage system. **Applied Thermal Engineering**, v. 22, n. 15, p. 1705-1716, Oct. 2002.

DOI 10.1016/S1359-4311(02)00080-7.

ISMAIL, K. A. R. A. R.; STUGINSKY, R.; STUGINSKY JR, R. A parametric study on possible fixed bed models for pcm and sensible heat storage. **Applied Thermal Engineering**, v. 19, n. 7, p. 757-788, July 1999. DOI 10.1016/S1359-4311(98)00081-7.

IZQUIERDO-BARRIENTOS, M. A. et al. Experimental study of fixed and fluidized beds of PCM with an internal heat exchanger. **Applied Thermal Engineering**, v. 106, p. 1042-1051, Aug. 2016. DOI 10.1016/j.applthermaleng.2016.06.049.

KARTHIKEYAN, S. et al. Parametric studies on packed bed storage unit filled with PCM encapsulated spherical containers for low temperature solar air heating applications. **Energy Conversion and Management**, v. 78, p. 74-80, Feb. 2014. DOI 10.1016/j.enconman.2013.10.042.

KRISHNA, R. Adsorptive separation of CO2/CH4/CO gas mixtures at high pressures. **Microporous and Mesoporous Materials**, v. 156, p. 217-223, July 2012. DOI 10.1016/j.micromeso.2012.02.034.

LI, X.; LI, Y. Applications of organic phase change materials embedded in adsorbents for controlling heat produced by charging and discharging natural gas. **Adsorption**, v. 21, n. 5, p. 383-389, Feb. 2015. DOI 10.1007/s10450-015-9678-4.

LOPES, F. V. S.; GRANDE, C. A.; RODRIGUES, A. E. Fast-cycling VPSA for hydrogen purification. **Fuel**, v. 93, p. 510-523, Mar. 2012. DOI 10.1016/j.fuel.2011.07.005.

MAGALHÃES SIQUEIRA, R. et al. Simple procedure to estimate mass transfer coefficients from uptake curves on activated carbons. **Chemical Engineering & Technology**, v. 41, n. 8, p. 1622-1630, Aug. 2018. DOI 10.1002/ceat.201800091.

MARTIN-ROBERTS, E. et al. Carbon capture and storage at the end of a lost decade. **One Earth**, v. 4, n. 11, p. 1569-1584, Nov. 2021. DOI 10.1016/j.oneear.2021.10.002.

MEDVEĎ, I.; ČERNÝ, R. Surface diffusion in porous media: A critical review. **Microporous and Mesoporous Materials**, v. 142, n. 2-3, p. 405-422, July 2011. DOI 10.1016/j.micromeso.2011.01.015.

MOKHATAB, S.; POE, W. A.; MAK, J. Y. **Natural gas dehydration and mercaptans removal**. Handb. Nat. Gas Transm. Process. [S.l.]: Elsevier, 2019. 348 p.

MOTA, J. P. **Adsorbed natural gas technology**. Recent Adv. Adsorpt. Process. Environ. Prot. Secur. Dordrecht: Springer Netherlands, 2008. p. 192.

NAGANO, K. et al. Thermal characteristics of a direct heat exchange system between granules with phase change material and air. **Applied Thermal Engineering**, v. 24, n. 14-15, p. 2131-2144, Oct. 2004. DOI 10.1016/S1359-4311(02)00161-8.

NALLUSAMY, N.; SAMPATH, S.; VELRAJ, R. Experimental investigation on a combined

sensible and latent heat storage system integrated with constant/varying (solar) heat sources. **Renewable Energy**, v. 32, n. 7, p. 1206-1227, June 2007. DOI 10.1016/j.renene.2006.04.015.

NALLUSAMY, N.. Study on performance of a packed bed latent heat thermal energy storage unit integrated with solar water heating system. **Journal of Zhejiang University-SCIENCE A**, v. 7, n. 8, p. 1422-1430, Aug. 2006. DOI 10.1631/jzus.2006.A1422.

NOËL, J. A. et al. **Phase change materials**. Storing Energy. [S.l.]: Elsevier, 2016. p. 272 p.

PATEL, H. Fixed-bed column adsorption study: a comprehensive review. **Applied Water Science**, v. 9, n. 3, p. 45, Apr. 2019. DOI 10.1007/s13201-019-0927-7.

PAUSE, B. **Phase change materials and their application in coatings and laminates for textiles**. Smart Text. Coatings Laminates. [S.l.]: Elsevier, 2019. 187 p.

POURHAKKAK, P. et al. **Fundamentals of adsorption technology**. Interface Science and Technology. [S.l: s.n.], 2021. 70 p.

PRADO, D. S. et al. Functionally graded optimisation of adsorption systems with phase change materials. **Structural and Multidisciplinary Optimization**, v. 64, n. 2, p. 473-503, Aug. 2021. DOI 10.1007/s00158-021-02918-y.

QIU, H. et al. Critical review in adsorption kinetic models. **Journal of Zhejiang University-SCIENCE A**, v. 10, n. 5, p. 716-724, Aug. 2009. DOI 10.1631/jzus.A0820524.

RACKLEY, S. A. **Adsorption capture systems**. Carbon capture and storage. [S.l.]: Elsevier, 2010. 157 p.

RADY, M. Thermal performance of packed bed thermal energy storage units using multiple granular phase change composites. **Applied energy**, v. 86, n. 12, p. 2704-2720, Dec. 2009. DOI 10.1016/j.apenergy.2009.04.027.

RAHMAN, K. A. et al. Thermal enhancement of charge and discharge cycles for adsorbed natural gas storage. **Applied Thermal Engineering**, v. 31, n. 10, p. 1630-1639, July 2011. DOI 10.1016/j.applthermaleng.2011.02.002.

RAY, S.; DAS, G. **Adsorption**. Process Equip. Plant Des. [S.l.]: Elsevier, 2020. 384 p.

REGIN, A. F.; SOLANKI, S. C.; SAINI, J. S. Heat transfer characteristics of thermal energy storage system using PCM capsules: a review. **Renewable and Sustainable Energy Reviews**, v. 12, n. 9, p. 2438-2458, Dec. 2008. DOI 10.1016/j.rser.2007.06.009.

RUTHVEN, D. M. **Adsorption, fundamentals.** Kirk-Othmer Encycl. Chem. Technol. Hoboken, NJ, USA: John Wiley & Sons, Inc., 2001; 36 p.

RUTHVEN, D. M.; XU, Z. Diffusion of oxygen and nitrogen in 5A zeolite crystals and commercial 5A pellets. **Chemical Engineering Science**, v. 48, n. 18, p. 3307-3312, Sept. 1993. DOI 10.1016/0009-2509(93)80214-B.

SAKANAKA, Y. et al. Efficiency of thermal management using phase-change material for nonisothermal adsorption process. **Industrial & Engineering Chemistry Research**, v. 59, n. 32, p. 14485-14495, Aug. 2020. DOI 10.1021/acs.iecr.0c02344.

SAMANTA, A. et al. Post-combustion CO2 capture using solid sorbents: a review. **Industrial & Engineering Chemistry Research**, v. 51, n. 4, p. 1438-1463, Feb. 2012. DOI 10.1021/ie200686q.

SCHUMANN, T. E. W. Heat transfer: A liquid flowing through a porous prism. **Journal of the Franklin Institute**, v. 208, n. 3, p. 405-416, Sept. 1929. DOI 10.1016/S0016-0032(29)91186-8.

SHAH, G. et al. **Recent developments in pressure swing adsorption for biomethane production**. Emerg. Technol. Biol. Syst. Biogas Upgrad. [S.l.]: Elsevier, 2021. 116 p.

SHARMA, A. et al. Review on thermal energy storage with phase change materials and applications. **Renewable and Sustainable Energy Reviews**, v. 13, n. 2, p. 318-345, Feb. 2009. DOI 10.1016/j.rser.2007.10.005.

SIRCAR, S.; HUFTON, J. R. Why does the linear driving force model for adsorption kinetics work? **Adsorption**, v. 6, n. 2, p. 137-147, Aug. 2000. DOI 10.1023/A:1008965317983.

SIRIWARDANE, R. V. et al. Adsorption of CO2 on molecular sieves and activated carbon. **Energy & Fuels**, v. 15, n. 2, p. 279-284, Mar. 2001. DOI 10.1021/ef000241s.

TOLEDO, M. et al. Use of phase change materials on an adsorbed carbon dioxide storage system. **Applied Thermal Engineering**, v. 51, n. 1-2, p. 512-519, Mar. 2013. DOI 10.1016/j.applthermaleng.2012.09.034.

VEMULA, R. R.; SIRCAR, S. Comparative performance of an adiabatic and a nonadiabatic PSA process for bulk gas separation-a numerical simulation. **AIChE Journal**, v. 63, n. 9, p. 4066-4078, Sept. 2017. DOI 10.1002/aic.15740.

WU, M.; XU, C.; HE, Y.-L. Dynamic thermal performance analysis of a molten-salt packed-bed thermal energy storage system using PCM capsules. **Applied Energy**, v. 121, p. 184-195, May 2014. DOI 10.1016/j.apenergy.2014.01.085.

WU, Shaofei et al. Thermal conductivity enhancement on phase change materials for thermal energy storage: A review. **Energy Storage Materials**, v. 25, p. 251-295, Mar. 2020. DOI

WU, Shuangmao; FANG, G. Dynamic performances of solar heat storage system with packed bed using myristic acid as phase change material. **Energy and Buildings**, v. 43, n. 5, p. 1091-1096, Aug. 2011. DOI 10.1016/j.ensm.2019.10.010.

XIA, L.; ZHANG, P.; WANG, R. Z. Numerical heat transfer analysis of the packed bed latent heat storage system based on an effective packed bed model. **Energy**, v. 35, n. 5, p. 2022-2032, Aug. 2010. DOI 10.1016/j.energy.2010.01.018.

YANG, R. T. **Adsorbents: fundamentals and applications**. Hoboken, NJ, USA, NJ, USA: John Wiley & Sons, Inc., 2003. 425 p.

YANG, X. D. et al. Experimental studies of the performance of adsorbed natural gas storage system during discharge. **Applied Thermal Engineering**, v. 25, n. 4, p. 591-601, Aug. 2005. DOI 10.1016/j.applthermaleng.2004.07.002.

ZALBA, B. et al. Review on thermal energy storage with phase change: materials, heat transfer analysis and applications. **Applied Thermal Engineering**, v. 23, n. 3, p. 251-283, Feb. 2003. DOI 10.1016/S1359-4311(02)00192-8.

ZANGANEH, G. et al. Stabilization of the outflow temperature of a packed-bed thermal energy storage by combining rocks with phase change materials. **Applied Thermal Engineering**, v. 70, n. 1, p. 316-320, Sept. 2014. DOI 10.1016/j.applthermaleng.2014.05.020.

ZHANG, J. et al. Effect of flue gas impurities on CO2 capture performance from flue gas at coal-fired power stations by vacuum swing adsorption. **Energy Procedia**, v. 1, n. 1, p. 1115-1122, Aug. 2009. DOI 10.1016/j.egypro.2009.01.147.

ZIMMERMANN, W.; KELLER, J. U. Enhancement of adsorption capacity by use of phase change material (pcm) as additive in an activated carbon (ac) fixed bed adsorber. In: LOUREIRO, J. M.; KARTEL, M. T. (Org.). **Combining hybrid adsorbents.** Dordrecht: Springer Netherlands. p. 219-224, Aug. 2006. DOI 10.1007/1-4020-5172-7_24.

Appendix I

Note: The MATLAB® is coupled with COMSOL Multiphysics®.

- Code for variables:

```
%variables code
%
%set data
global P_column;
P_column = 6; %operation pressure [bar]
global y_CO2;
y_CO2 = 0.2; %inlet CO2 molar fraction [dimensionless]
global Q;
Q = 1.7e-5; %inlet volumetric flow [(m^3)/s]
global D_int;
D_int = 0.028; %bed internal diameter [m]
global L;
L = 0.4; %bed length [m]
global time;
time = 1200; %process time [s]
global N_pcm;
N_pcm = 1.*(12); %quantity of PCM capsules [dimensionless]
global time_set;
time_set = 1000; %time for 90% C/C0

%fluid phase data
global T_gin;
T_gin = 20+273; %inlet gas temperature [K]
global MM_CO2;
MM_CO2 = 44; %CO2 molar mass [g/mol]
global MM_N2;
MM_N2 = 28; %N2 molar mass [g/mol]
global Cp_CO2;
Cp_CO2 = 36.475; %CO2 molar specific heat at constant pressure (T=273K) [J/mol.K]
global Cp_N2;
Cp_N2 = 29.15; %N2 molar specific heat at constant pressure (T=273K) [J/mol.K]
global Cv_CO2;
Cv_CO2 = 27.8; %CO2 molar specific heat at constant volume (T=273K) [J/mol.K]
global Cv_N2;
Cv_N2 = 20.8; %N2 molar specific heat at constant volume (T=273K) [J/mol.K]
global Mu_CO2;
Mu_CO2 = 13.71e-6; %CO2 dynamic viscosity (P=1bar,T=273K) [Pa.s]
global Mu_N2;
Mu_N2 = 16.65e-6; %N2 dynamic viscosity (P=1bar,T=273K) [Pa.s]
global Dm_CO2;
Dm_CO2 = 2.7813e-6; %CO2 molecular diffusivity (?) [(m^2)/s]
global Dm_N2;
Dm_N2 = 9.5813e-6; %N2 molecular diffusivity (?) [(m^2)/s]
global k_CO2;
k_CO2 = 14.7e-3; %CO2 thermal conductivity (P=1bar,T=273K) [W/m.K]
global k_N2;
k_N2 = 24e-3; %N2 thermal conductivity (P=1bar,T=273K) [W/m.K]
global R_gas;
R_gas = 8.314; %ideal gas constant [L.kPa/K.mol]
%bed data
global y0_CO2;
y0_CO2 = 0; %initial CO2 molar fraction [dimensionless]
global y0_N2;
y0_N2 = 1; %initial N2 molar fraction [dimensionless]
global E;
E = 0.52; %bed porosity [dimensionless] NORITRB4
%adsorbent phase data
global D_p;
D_p = 3.5e-3; %adsorbent particle diameter [m]
global p_p;
p_p = (1).*(471e3); %adsorbent particle density [g/m^3]
```

```
global C_s;
C_s = (1).*(820e-3); %adsorbent specific heat [J/g.K] http://dx.doi.org/10.3390/e22080808
global k_s;
k_s = 1.5; %adsorbent thermal conductivity [W/m.K] http://dx.doi.org/10.1088/1757-899X/502/1/012197
%PCM cylindrical capsule data:
global tol;
tol = 0.01; %PCM lenght tolerance in bed [m]
global L_pcm;
L_pcm = L - tol; %PCM capsule lenght [m]
global t_capsule;
t_capsule = 0.1e-3; %PCM capsule wall thickness [m]
%
global D_capsule;
D_capsule = 2e-3; %PCM capsule external diameter [m]
global D_pcm;
D_pcm = D_capsule-2.*t_capsule; %PCM capsule internal diameter [m]
%
%PCM HEAT TRANSFER
global h_pcm;
h_pcm = 60; %PCM-bed heat transfer coefficient [W/K.m^2]
%
%PCM PARAFFIN properties
global p_pcm;
p_pcm = 790; %PCM density [kg/m^3]
global C_pcm;
C_pcm = 2890; %PCM specific heat [J/kg.K]
global k_pcm;
k_pcm = 0.24; %PCM thermal conductivity [W/m.K]
global T_melt;
T_melt = 27+273; %PCM melting temperature [K]
global DH_melt;
DH_melt = 250e3; %PCM melting enthalpy [J/kg]
%{
%PCM ACID properties
global p_pcm;
p_pcm = 950; %PCM density [kg/m^3]
global C_pcm;
C_pcm = 2100; %PCM specific heat [J/kg.K]
global k_pcm;
k_pcm = 0.24; %PCM thermal conductivity [W/m.K]
global T_melt;
T_melt = 27+273; %PCM melting temperature [K]
global DH_melt;
DH_melt = 125e3; %PCM melting enthalpy [J/kg]
%
%
%PCM GENERIC properties
global p_pcm;
p_pcm = 1000; %PCM density [kg/m^3]
global C_pcm;
C_pcm = 2500; %PCM specific heat [J/kg.K]
global k_pcm;
k_pcm = 0.24; %PCM thermal conductivity [W/m.K]
global T_melt;
T_melt = 27+273; %PCM melting temperature [K]
global DH_melt;
DH_melt = 100e3; %PCM melting enthalpy [J/kg]
%}
%
%LDF model data
global kldf_CO2;
kldf_CO2 = (1).*0.1; %rate constant (for instantaneous adsorption process) [1/s]
global kldf_N2;
kldf_N2 = (1).*0.05; %rate constant (for instantaneous adsorption process) [1/s]
%toth isotherm data
global DH_CO2;
DH_CO2 = (1).*(-25e3); %CO2 adsorption enthalpy toth model [J/mol]
global DH_N2;
DH_N2 = (1).*(-16e3); %N2 adsorption enthalpy toth model [J/mol]
global K0_CO2;
K0_CO2 = (1).*(76.2e-6); %CO2 equilibrium constant toth model [1/bar]
```

```
global K0_N2;
K0_N2 = 69.1e-6; %N2 equilibrium constant toth model [1/bar]
global qm_CO2;
qm_CO2 = (1).*0.01005; %CO2 adsorption capacity constant toth model [mol/g]
global qm_N2;
qm_N2 = 0.00974; %N2 adsorption capacity constant toth model [mol/g]
global n_CO2;
n_CO2 = 0.68; %CO2 heterogeneity parameter toth model [dimensionless]
global n_N2;
n_N2 = 0.52; %N2 heterogeneity parameter toth model [dimensionless]
%wall data
global l;
l = 0.18e-2; %wall thickness [m]
global Cp_w;
Cp_w = 500; %wall specific heat at constant pressure [J/kg.K]
global p_w;
p_w = 8238; %wall density [kg/m.^3]
global k_w;
k_w = 14.4; %wall thermal conductivity [W/m.K]
global Tw_avg;
Tw_avg = 25.1+273; %wall external surface average temperature [K]
%external air data
global T_amb;
T_amb = 20+273; %ambient temperature [K]
global a_air;
a_air = 22.15e-6; %ambient air thermal diffusivity [(m.^2)/s]
global b_air;
b_air = 3.363e-3; %ambient air isobar thermal expansion coefficient [K.^-1]
global v_air;
v_air = 15.822e-6; %ambient air kinematic viscosity [(m.^2)/s]
global kg_ext;
kg_ext = 26.84e-3; %ambient air thermal conductivity [W/m.K]
global g;
g = 9.81; %local gravitational acceleration [m/(s.^2)]
%special numbers
global pi;
pi = 3.1416; %pi number
global euler;
euler = 2.7183; %euler number
global key;
key = 10.^(50); %heaviside step-function constant
global delt;
delt = 10.^(-4); %heaviside step-function displacement
%calculating paramaters
global y_N2;
y_N2 = (1 - y_CO2); %inlet N2 molar fraction [dimensionless]
global V_column;
V_column = L.*(pi.*(D_int.^2)./4)*(10.^3); %column internal volume [L]
global P_gas;
P_gas = P_column*(10.^2); %gas phase pressure [kPa]
global D_ext;
D_ext = (D_int + l); %bed external diameter [m]
global V_pcm;
V_pcm = pi.*((D_pcm.^2)./4).*L_pcm; %PCM volume [m^3]
global V_capsule;
V_capsule = pi*((D_capsule^2)./4)*L_pcm; %PCM capsule volume [m^3]
global A_capsule;
A_capsule = pi*D_capsule*L_pcm; %PCM capsule surface area [m^2]
global omega_pcm;
omega_pcm = (N_pcm*V_pcm)./(V_column*(10.^-3)); %PCM dilution factor within bed [adimensinal]
global phi_bed;
phi_bed = (N_pcm*V_capsule)./(V_column*(10.^-3)); %adsorption bed complementary volume fraction
[dimensionless]
global alpha_pcm;
alpha_pcm = (N_pcm*A_capsule)./(V_column*(10.^-3)); %rational of PCM capsules surface area to
column volume [m^-1]
global psi_bed;
psi_bed = (N_pcm.*pi.*((D_capsule.^2)./4))./(pi.*((D_int.^2)./4)); %rational of PCM capsules cross
section area to bed cross section area [dimensionless]
global u_s;
u_s = (4.*Q)./((1-psi_bed).*pi.*(D_int.^2)); %superficial velocity [m/s]
```

```
global MM_g;
MM_g = ((y_CO2.*MM_CO2) + (y_N2.*MM_N2)); %gas phase molar mass [g/mol]
global p_g;
p_g = (P_gas/(R_gas*T_amb))*MM_g; %gas phase density [kg/(m^3)]
global fv_pcm;
fv_pcm = (N_pcm.*V_pcm)./(V_column*(10.^-3)); %PCM volume fraction [dimensionless]
global fv_capsule;
fv_capsule = (N_pcm.*V_capsule)./(V_column*(10.^-3)); %PCM capsule volume fraction [dimensionless]
global fv_copper;
fv_copper = (fv_capsule-fv_pcm); %copper volume fraction [dimensionless]
global ratio_copper;
ratio_copper = (fv_copper./fv_capsule); %ratio of copper volume to PCM capsule volume
[dimensionless]
global Biot_pcm;
Biot_pcm = (h_pcm./k_pcm)*(D_pcm./2); %PCM internal heat transfer parameter [dimensionless]
global M_ads;
M_ads = ((V_column.*(10.^-3)) - (N_pcm.*V_capsule)).*(1-E).*(p_p.*(10.^-3)); %adsorbent mass [kg]
global V_gas;
V_gas = (V_column - (N_pcm.*(10.^3).*V_capsule)).*E; %non-adsorbed gas volume [L]
global M_gas;
M_gas = (V_gas.*(10.^-3)).*p_g; %non-adsorbed gas mass [kg]
global M_pcm;
M_pcm = (N_pcm.*V_pcm).*p_pcm; %PCM mass [kg]
global M_total;
M_total = M_ads + M_gas + M_pcm; %total adsorption bed mass [kg]
global x_ads;
x_ads = M_ads/M_total; %adsorbent mass fraction [dimensionless]
global x_gas;
x_gas = M_gas/M_total; %non-adsorbed gas mass fraction [dimensionless]
global x_pcm;
x_pcm = M_pcm/M_total; %PCM mass fraction [dimensionless]
global Cv_g;
Cv_g = ((y_CO2.*Cv_CO2) + (y_N2.*Cv_N2)); %gas phase specific heat at constant volume [J/mol.K]
global Cp_g;
Cp_g = ((y_CO2.*Cp_CO2) + (y_N2.*Cp_N2)); %gas phase specific heat at constant pressure [J/mol.K]
global kg;
kg = ((y_CO2.*k_CO2) + (y_N2.*k_N2)); %gas phase thermal conductivity [W/m.K]
global Dm_g;
Dm_g = ((y_CO2.*Dm_CO2) + (y_N2.*Dm_N2)); %gas phase molecular diffusivity [(m^2)/s]
global Mu_g;
Mu_g = ((y_CO2.*Mu_CO2) + (y_N2.*Mu_N2)); %gas phase dynamic viscosity [Pa.s]
global Re;
Re = (p_g.*u_s.*D_p)./(Mu_g); %reynolds number [dimensionless]
global Pr;
Pr = (Cp_g.*Mu_g)./(kg); %prandtl number [dimensionless]
global Sc;
Sc = (Mu_g)./(p_g.*Dm_g); %schmidt number [dimensionless]
global Nu;
Nu = 2.0 + 1.1.*(Re.^(0.6)).*(Pr.^(1/3)); %nusselt number [dimensionless]
global E0; %stagnant contribution to axial dispersion [dimensionless]
if (Re > 0 && Re <= 1)
   E0 = 0.23;
elseif (Re >= 10)
   E0 = 20;
else
   E0 = (20 - ((10-Re).*((20-0.23)./(10-1))));
end
global h_f;
h_f = ((Nu.*kg)./D_p); %solid phase heat transfer coefficient [W/K.m^2]
global D_L;
D_L = (E0+(0.5.*Sc.*Re)).*(Dm_g./E); %bed axial mass dispersion coefficient [(m^2)/s]
global lamb_L;
lamb_L = (kg)*(7+(0.5.*Pr.*Re)); %bed axial thermal dispersion coefficient [W/m.K]
global h_w;
h_w = (12.5+(0.048.*Re))*(kg./D_int); %internal wall heat transfer coefficient [W/K.m^2]
global Ra;
Ra = (g.*b_air.*(Tw_avg-T_amb).*(L.^3))/(v_air.*a_air); %rayleigh number [dimensionless]
global h_ext;
h_ext = (0.68+(0.67.*(Ra.^(1./4))/((1+((0.492./Pr).^(9./12))).^(4./16)))).*(kg_ext./L); %external
convective heat transfer coefficient [W/K.m^2]
global U;
```

```
U   =   1./((1./h_w)+((D_int./k_w).*(log(D_ext./D_int)))+((D_int./D_ext).*(1./h_ext)));   %external
global heat transfer coefficient [W/K.m^2]
global alpha_w;
alpha_w = D_int./(l.*(D_int+l)); %rational of internal surface area to column wall volume [m^-1]
global alpha_wl;
alpha_wl = 1./((D_int+l).*(log((D_int+l)./(D_int)))); %rational of collumn shell logarithmic mean
surface area to column wall volume [m^-1]
```

- Main code:

```
%PCM axial fixed bed model
adspcm_variables;
%modelling
x = linspace(0,L,50);%(z=0,z=L,discretization=L/50)
t = linspace(0,time,time);%(t=0,t=time,discretization=time/time)
m = 0;
sol = pdepe(m,@heatpde,@heatic,@heatbc,x,t);
u1 = sol(:,:,1);
u2 = sol(:,:,2);
u3 = sol(:,:,3);
u4 = sol(:,:,4);
u5 = sol(:,:,5);
u6 = sol(:,:,6);
u7 = sol(:,:,7);
u8 = sol(:,:,8);
u9 = sol(:,:,9);
u10 = sol(:,:,10);
%{
figure
surf(x,t,(u1) + (u2))
xlabel('z (m)')
ylabel('t (s)')
zlabel('C_g(z,t) (mol/m^3)')
view([150 25])
%
figure
surf(x,t,u3)
xlabel('z (m)')
ylabel('t (s)')
zlabel('T_g (z,t) (K)')
view([150 25])
%
figure
surf(x,t,u10)
xlabel('z (m)')
ylabel('t (s)')
zlabel('u_s(z,t) (m/s)')
view([150 25])
%
figure
surf(x,t,u1)
xlabel('z (m)')
ylabel('t (s)')
zlabel('C_CO2 (z,t) (mol/m^3)')
view([150 25])
%
figure
surf(x,t,u2)
xlabel('z (m)')
ylabel('t (s)')
zlabel('C_N2 (z,t) (mol/m^3)')
view([150 25])
%
figure
surf(x,t,u4)
xlabel('z (m)')
ylabel('t (s)')
zlabel('q_CO2 (z,t) (mol/g)')
view([150 25])
%
figure
```

```
surf(x,t,u5)
xlabel('z (m)')
ylabel('t (s)')
zlabel('q_N2 (z,t) (mol/g)')
view([150 25])
%
figure
surf(x,t,u6)
xlabel('z (m)')
ylabel('t (s)')
zlabel('T_s (z,t) (K)')
view([150 25])
%
figure
surf(x,t,u7)
xlabel('z (m)')
ylabel('t (s)')
zlabel('T_w (z,t) (K)')
view([150 25])
%
figure
surf(x,t,u8)
xlabel('z (m)')
ylabel('t (s)')
zlabel('T_pcm (z,t) (K)')
view([150 25])
%
figure
surf(x,t,u9)
xlabel('z (m)')
ylabel('t (s)')
zlabel('X_melt (z,t)')
view([150 25])
%}
figure %gas temperature profile z=L
plot(t,sol(:,end,3))
xlabel('t (s)')
ylabel('T_g (K)')
title('Temperature change of gas phase at end of cylinder')
%{
figure
plot(t,sol(:,1,6))
xlabel('t (s)')
ylabel('T_s (K)')
title('Temperature change of solid phase at entrance of cylinder')
%
figure %adsorbent temperature profile z=L
plot(t,sol(:,end,6))
xlabel('t (s)')
ylabel('T_s (K)')
title('Temperature change of solid phase at end of cylinder')
%
figure
plot(t,u6(:,:))
xlabel('t (s)')
ylabel('T_s (K)')
title('Temperature change of solid phase at any distance')
%
figure
plot(x,u6(end,:))
xlabel('z (m)')
ylabel('T_s (K)')
title('Temperature profile of solid phase at final t')
%
figure
plot(t,sol(:,1,4))
xlabel('t (s)')
ylabel('q_CO2 (mol/g)')
title('CO2 adsorption change at entrance of cylinder')
%
figure %CO2 adsorbed z=L
```

```
plot(t,sol(:,end,4))
xlabel('t (s)')
ylabel('q_CO2 (mol/g)')
title('CO2 adsorption change at end of cylinder')
%
figure
plot(t,sol(:,1,5))
xlabel('t (s)')
ylabel('q_N2 (mol/g)')
title('N2 adsorption change at entrance of cylinder')
%
figure
plot(t,sol(:,end,5))
xlabel('t (s)')
ylabel('q_N2 (mol/g)')
title('N2 adsorption change at end of cylinder')
%
figure
plot(t,sol(:,end,7))
xlabel('t (s)')
ylabel('T_w (K)')
title('Temperature change of wall at end of cylinder')
%
figure
plot(t,u7(:,:))
xlabel('t (s)')
ylabel('T_w (K)')
title('Temperature change of wall at any distance')
%
figure %CO2 breakthrough curve
plot(t,(sol(:,end,1))./((sol(:,end,1)+sol(:,end,2))*y_CO2))
xlabel('t (s)')
ylabel('C/C_0')
title('Breakthrough Curve CO_2')
%}
figure %pcm temperature profile z=L
plot(t,sol(:,end,8))
xlabel('t (s)')
ylabel('T_pcm (K)')
title('Temperature change of PCM at end of cylinder')
%{
figure %pcm molten fraction z=L
plot(t,sol(:,end,9))
xlabel('t (s)')
ylabel('X_pcm')
title('PCM Molten Fraction change at end of cylinder')
%}
%CO2 moles adsorbed (total)
V_ads = (V_column - (N_pcm.*(10.^3).*V_capsule)).*(1-E); %solid phase volume [L]
%
integral_adsorption_CO2_1 = (p_p.*V_ads).*((trapz(x,u4(time_set,:)))./L);
display(integral_adsorption_CO2_1) %number of mol adsorbed [mol]
%
function [c, f, s] = heatpde(x,t,u,dudx)
%set data
global P_column;
global y_CO2;
global Q;
global N_pcm;
%fluid phase data
global T_gin;
global MM_CO2;
global MM_N2;
global Cp_CO2;
global Cp_N2;
global Cv_CO2;
global Cv_N2;
global Mu_CO2;
global Mu_N2;
global Dm_CO2;
global Dm_N2;
```

```
global k_CO2;
global k_N2;
global R_gas;
%bed data
global y0_CO2;
global y0_N2;
global E;
global D_int;
global L;
%adsorbent phase data
global D_p;
global p_p;
global C_s;
global k_s;
%PCM cylindrical capsule data:
global tol;
global L_pcm;
global t_capsule;
%
global D_capsule;
global D_pcm;
%
%PCM HEAT TRANSFER
global h_pcm;
%
%PCM properties
global p_pcm;
global C_pcm;
global k_pcm;
global T_melt;
global DH_melt;
%}
%
%LDF model data
global kldf_CO2;
global kldf_N2;
%toth isotherm data
global DH_CO2;
global DH_N2;
global K0_CO2;
global K0_N2;
global qm_CO2;
global qm_N2;
global n_CO2;
global n_N2;
%wall data
global l;
global Cp_w;
global p_w;
global k_w;
global Tw_avg;
%external air data
global T_amb;
global a_air;
global b_air;
global v_air;
global kg_ext;
global g;
%special numbers
global pi;
global euler;
global key;
global delt;
%calculating paramaters
global y_N2;
global V_column;
global P_gas;
global D_ext;
global V_pcm;
global V_capsule;
global A_capsule;
```

```
global omega_pcm;
global phi_bed;
global alpha_pcm;
global psi_bed;
global u_s;
global MM_g;
global p_g;
global fv_pcm;
global fv_capsule;
global fv_copper;
global ratio_copper;
global Biot_pcm;
global M_ads;
global V_gas;
global M_gas;
global M_pcm;
global M_total;
global x_ads;
global x_gas;
global x_pcm;
global Cv_g;
global Cp_g;
global kg;
global Dm_g;
global Mu_g;
global Re;
global Pr;
global Sc;
global Nu;
global E0;
global h_f;
global D_L;
global lamb_L;
global h_w;
global Ra;
global h_ext;
global U;
global alpha_w;
global alpha_wl;
%partial differential equations
c = [(1).*E; (1).*E; (1).*(E*(P_gas/(R_gas*u(3)))*(10^3)*(Cv_g)); (1).*1; (50).*1;
(5).*(p_p*C_s); (1).*(p_w*Cp_w); (1).*(omega_pcm*p_pcm*C_pcm); (1).*(omega_pcm*p_pcm*DH_melt);
(1).*0]; %BM_CO2 (C_CO2); BM_N2 (C_N2); BE_gas (T_g); LDF_CO2 (q_CO2); LDF_N2 (q_N2); BE_solid
(T_s); BE_wall (T_w); BE_pcm (T_pcm); BM_pcm (X_melt); Continuity (u_s) [equation / variable]
f = [(E*D_L).*dudx(1); (E*D_L).*dudx(2); E*lamb_L.*dudx(3); 0; 0; 0; 0; 0; 0; 0];
s = [(-(u(10)*dudx(1) + dudx(10)*u(1))) + (-(1-E)*p_p*(kldf_CO2*(((qm_CO2*K0_CO2*(euler^(-
DH_CO2/(R_gas*u(6))))*P_column*(u(1)/(u(1)+u(2))))/((1 + (K0_CO2*(euler^(-
DH_CO2/(R_gas*u(6))))*P_column*(u(1)/(u(1)+u(2))))^n_CO2)^(1/n_CO2)))-u(4)))); (-(u(10)*dudx(2) +
dudx(10)*u(2))) + (-(1-E)*p_p*(kldf_N2*(((qm_N2*K0_N2*(euler^(-
DH_N2/(R_gas*u(6))))*P_column*(u(2)/(u(1)+u(2))))/((1 + (K0_N2*(euler^(-
DH_N2/(R_gas*u(6))))*P_column*(u(2)/(u(1)+u(2))))^n_N2)^(1/n_N2)))-u(5)))); (-
(P_gas/(R_gas*u(3)))*(10^3)*(Cp_g)*(u(10)*dudx(3) + dudx(10)*u(3))) + ((1-E)*((6*h_f)/D_p)*(u(6)-
u(3))) + (-((4*h_w)/(D_int*(1-phi_bed)))*(u(3)-u(7))); kldf_CO2*(((qm_CO2*K0_CO2*(euler^(-
DH_CO2/(R_gas*u(6))))*P_column*(u(1)/(u(1)+u(2))))/((1 + (K0_CO2*(euler^(-
DH_CO2/(R_gas*u(6))))*P_column*(u(1)/(u(1)+u(2))))^n_CO2)^(1/n_CO2)))-u(4));
kldf_N2*(((qm_N2*K0_N2*(euler^(-DH_N2/(R_gas*u(6))))*P_column*(u(2)/(u(1)+u(2))))/((1 +
(K0_N2*(euler^(-DH_N2/(R_gas*u(6))))*P_column*(u(2)/(u(1)+u(2))))^n_N2)^(1/n_N2)))-u(5)); (-
((6*h_f)/D_p)*(u(6)-u(3))) + ((p_p)*((-DH_CO2*(kldf_CO2*(((qm_CO2*K0_CO2*(euler^(-
DH_CO2/(R_gas*u(6))))*P_column*(u(1)/(u(1)+u(2))))/((1 + (K0_CO2*(euler^(-
DH_CO2/(R_gas*u(6))))*P_column*(u(1)/(u(1)+u(2))))^n_CO2)^(1/n_CO2)))-u(4)))) + (-
DH_N2*(kldf_N2*(((qm_N2*K0_N2*(euler^(-DH_N2/(R_gas*u(6))))*P_column*(u(2)/(u(1)+u(2))))/((1 +
(K0_N2*(euler^(-DH_N2/(R_gas*u(6))))*P_column*(u(2)/(u(1)+u(2))))^n_N2)^(1/n_N2)))-u(5))))) +
((1-(1/(1+(euler^(-2*key*(u(8)-(T_melt-delt))))))))*(((-h_pcm*alpha_pcm)/((1-E)*(1-
phi_bed)))*(u(6)-u(8)))) + ((1-(1/(1+(euler^(-2*key*(u(9)-(1-delt))))))))*(1/(1+(euler^(-
2*key*(u(8)-(T_melt-delt))))))*(((-h_pcm*alpha_pcm)/((1-E)*(1-phi_bed)))*(u(6)-T_melt))) +
((1/(1+(euler^(-2*key*(u(9)-(1-delt))))))*(((-h_pcm*alpha_pcm)/((1-E)*(1-phi_bed)))*(u(6)-
T_melt))); (alpha_w*h_w*(u(3)-u(7))) + (-alpha_wl*U*(u(7)-T_amb)); ((1-(1/(1+(euler^(-
2*key*(u(8)-(T_melt-delt))))))))*(h_pcm*alpha_pcm)*(u(6)-u(8))) + ((1/(1+(euler^(-2*key*(u(9)-(1-
delt))))))*(h_pcm*alpha_pcm)*(u(6)-u(8))); ((1-(1/(1+(euler^(-2*key*(u(9)-(1-
delt))))))))*(1/(1+(euler^(-2*key*(u(8)-(T_melt-delt))))))*(h_pcm*alpha_pcm)*(u(6)-T_melt)); (-((-
(P_gas/(R_gas*u(3)))*(10^3)*(Cp_g)*(u(10)*dudx(3) + dudx(10)*u(3))) + ((1-E)*((6*h_f)/D_p)*(u(6)-
```

```
u(3))) + (-((4*h_w)/(D_int*(1-phi_bed)))*(u(3)-u(7))))/(Cv_g*u(3)))  +  ((-
(P_gas/(R_gas*((u(3))^2)))*(10^3)*(dudx(3))*(u(10))) + (u(1)+u(2))*dudx(10)) - ((-(1-
E)*p_p*(kldf_CO2*(((qm_CO2*K0_CO2*(euler^(-DH_CO2/(R_gas*u(6))))*P_column*(u(1)/(u(1)+u(2))))/((1
+ (K0_CO2*(euler^(-DH_CO2/(R_gas*u(6))))*P_column*(u(1)/(u(1)+u(2))))^n_CO2)^(1/n_CO2)))-u(4))))
+ (-(1-E)*p_p*(kldf_N2*(((qm_N2*K0_N2*(euler^(-
DH_N2/(R_gas*u(6))))*P_column*(u(2)/(u(1)+u(2))))/((1 + (K0_N2*(euler^(-
DH_N2/(R_gas*u(6))))*P_column*(u(2)/(u(1)+u(2))))^n_N2)^(1/n_N2)))-u(5)))))];
end
function u0 = heatic(x)
%set data
global P_column;
global Q;
global N_pcm;
%fluid phase data
global R_gas;
%bed data
global y0_CO2;
global y0_N2;
global D_int;
%PCM cylindrical capsule data:
global t_capsule;
global D_capsule;
global D_pcm;
%toth isotherm data
global DH_CO2;
global DH_N2;
global K0_CO2;
global K0_N2;
global qm_CO2;
global qm_N2;
global n_CO2;
global n_N2;
%external air data
global T_amb;
global g;
%special numbers
global euler;
%calculating paramaters
global P_gas;
global psi_bed;
global u_s;
%initial conditions
u0 = [(y0_CO2*(P_gas/(R_gas*T_amb))*(10^3)); (y0_N2*(P_gas/(R_gas*T_amb))*(10^3)); 20+273;
((qm_CO2*K0_CO2*(euler^(-DH_CO2/(R_gas*T_amb)))*P_column*y0_CO2)/((1 + (K0_CO2*(euler^(-
DH_CO2/(R_gas*T_amb)))*P_column*y0_CO2)^n_CO2)^(1/n_CO2))); ((qm_N2*K0_N2*(euler^(-
DH_N2/(R_gas*T_amb)))*P_column*y0_N2)/((1 + (K0_N2*(euler^(-
DH_N2/(R_gas*T_amb)))*P_column*y0_N2)^n_N2)^(1/n_N2))); 20+273; 20+273; 20+273; 0; u_s];
%BM_CO2 (C_CO2); BM_N2 (C_N2); BE_gas (T_g); LDF_CO2 (q_CO2); LDF_N2 (q_N2); BE_solid (T_s);
BE_wall (T_w); Continuity (u_s) [equation / variable]
%CO2 conc; N2 conc; column gas temp; ...; solid temp; pcm temp; pcm molten mass fraction;
velocity
end
function [pl,ql,pr,qr] = heatbc(xl,ul,xr,ur,t)
%set data
global P_column;
global y_CO2;
global Q;
global N_pcm;
%fluid phase data
global T_gin;
global MM_CO2;
global MM_N2;
global Cp_CO2;
global Cp_N2;
global Mu_CO2;
global Mu_N2;
global Dm_CO2;
global Dm_N2;
global k_CO2;
global k_N2;
global R_gas;
```

```
%bed data
global E;
global D_int;
%solid phase data
global D_p;
%PCM cylindrical capsule data:
global t_capsule;
global D_capsule;
global D_pcm;
%external air data
global T_amb;
global g;
%special numbers
global pi;
%calculating paramaters
global y_N2;
global psi_bed;
global u_s;
global P_gas;
global MM_g;
global p_g;
global Cp_g;
global kg;
global Dm_g;
global Mu_g;
global Re;
global Pr;
global Sc;
global E0;
global D_L;
global lamb_L;
%boundary conditions
pl = [u_s*((y_CO2*(P_gas/(R_gas*T_gin))*(10^3))-ul(1)); u_s*((y_N2*(P_gas/(R_gas*T_gin))*(10^3))-
ul(2)); u_s*((P_gas/(R_gas*ul(3)))*(10^3))*Cp_g*(T_gin-ul(3)); 0; 0; 0; 0; 0; 0;
((P_gas/(R_gas*ul(3)))*(10^3))*ul(10) - u_s*((P_gas/(R_gas*T_gin))*(10^3))];
%
ql = [1; 1; 1; 1; 1; 1; 1; 1; 1; 0];
pr = [0; 0; 0; 0; 0; 0; 0; 0; 0; 0];
qr = [1; 1; 1; 1; 1; 1; 1; 1; 1; 1];
end
```